Forschungszentrum Karlsruhe

Technik und Umwelt

Wissenschaftliche Berichte

FZKA 6602

Analysis of a Thermite Experiment to Study Low Pressure Corium Dispersion

D. Wilhelm

Institut für Kern- und Energietechnik
Programm Nukleare Sicherheitsforschung

Forschungszentrum Karlsruhe GmbH, Karlsruhe
2001

Impressum der Print-Ausgabe:

Als Manuskript gedruckt

Forschungszentrum Karlsruhe GmbH
Postfach 3640, 76021 Karlsruhe

Mitglied der Hermann von Helmholtz-Gemeinschaft
Deutscher Forschungszentren (HGF)

ISSN 0947-8620

Analysis of a Thermite Experiment to Study Low Pressure Corium Dispersion

Abstract

The report describes the recalculation of a thermite experiment in a reduced scale which simulates the discharge of molten core materials out of the pressure vessel of a light water reactor into the open compartments and the dome of the containment. The experiment was performed in the framework of a multinational effort at the Sandia National Laboratory, U.S.A. It is being followed by the DISCO program at the Forschungszentrum Karlsruhe. A computational fluid dynamics code was supplemented with specific models to recalculate the Sandia experiment in order to identify problem areas which need to be addressed in the future. Therefore, a first attempt was undertaken to extrapolate to reactor conditions. This was done in two steps to separate geometric from material scaling relationships. The study shows that important experimental results can be extrapolated according to general scaling laws but that there are sensitivities, especially when replacing thermite by corium. The results show a considerable scatter and a dependence on geometric resolution and dynamics of energy transfer between participating components.

Analyse eines Thermitexperimentes für die Studie der Coriumdispersion bei niedrigem Druck

Zusammenfassung

Der Bericht beschreibt die Berechnung eines in reduziertem Maßstab durchgeführten Thermitexperimentes, das den Auswurf von geschmolzenem Kernmaterial aus dem Druckbehälter eines Leichtwasserreaktors in die angrenzenden Räume und den Dom des Sicherheitsbehälters beschreibt. Das Experiment wurde im Rahmen einer internationalen Übereinkunft im Sandia National Laboratory, U.S.A., durchgeführt. Die Thematik wird zur Zeit im DISCO Programm im Forschungszentrum Karlsruhe weiter verfolgt. Ein Fluiddynamikcode wurde mit speziellen Modellen ergänzt, um das Sandia Experiment nachzurechnen. Dabei wurden Problembereiche identifiziert, die zukünftig bearbeitet werden müssen. Ein erster Versuch der Extrapolation auf den Reaktorfall wurde unternommen. Die Extrapolation wurde in zwei Schritten durchgeführt, um die geometrische von der Materialskalierung zu trennen. Die Studie zeigt, daß wichtige experimentelle Resultate gemäß allgemeiner Skalierungsgesetze auf den Reaktorfall übertragen werden können, aber daß es Empfindlichkeiten vor allem beim Übergang von Thermit auf Corium gibt. Die Resultate unterliegen großen Abweichungen und Abhängigkeiten von der Geometrieauflösung und der Dynamik des Wärmeübergangs zwischen den verschiedenen Komponenten.

List of Contents Page

Executive Summary

In the event of a core melt-down of a pressurized water reactor, the molten metals and oxides may collect in the lower head of the pressure vessel. This report describes the analysis of a scaled-down thermite experiment performed at the Sandia National Laboratory, Albuquerque, which simulated the discharge of the melt through a given breach of the lower head driven by steam at a moderate pressure of 1.1 MPa.

Prior to this experiment, in a comprehensive program of the United States, the issue of direct containment heating was investigated. Equilibrium models and systems-level codes were successfully used to predict containment overpressures for different reactor types. The present program focuses on lower pressure levels in the vessel. Therefore, the containment overpressures and the fractions of melt discharged into the containment are lower. When focussing on where and when the melt is being dispersed, it became obvious that it was necessary to resolve, different to the previous studies, details of the geometry close to the breach. The present program not only seeks to provide results for the melt dispersion, but also for the time sequence of hydrogen generation, in-vessel pool behavior in the lower head, impact of the melt on safety components, and possibly also fission product distribution with the melt.

To a CFD code of the SIMMER family models were added which were found necessary to describe the phenomena during melt dispersion. The code was successfully used to recalculate all relevant physical quantities measured and to discuss effects and sensitivities of conditions which are not well known. Besides the achievement of a good agreement of the pressure transients, the main findings of the post-test analyses were confirmed, as there are a steam limited oxidation of metal in the cavity, a further oxidation in the containment, a constant hydrogen burning, and the limited amount of thermite dispersed beyond the cavity.

A first attempt was undertaken to extrapolate to prototypic condition. This was done in two steps, first to prototypic scale, and then from thermite to corium. While the geometric scale-up revealed only small differences to the experiment, especially in the dynamics, the change to corium showed new sensitivities. These depend on the specification of the melt, and are thus subjected to the history of the accident. By and large, the relevant results scale as predicted, the pressures look similar to the experiment except for the cavity pressures which are higher, the relative amount of hydrogen generated depends strongly on the melt mass and the metal content in the melt, and the fraction of melt discharged into the containment is lower but rather close to what has been measured. However, results show a considerable scatter and dependence with geometric resolution and dynamics of energy transfer between participating components. This underlines the demand for a more important number of thermite tests which will start in the DISCO facility of the Forschungszentrum Karlsruhe.

1 INTRODUCTION

If molten corium collected on the lower head of the reactor pressure vessel of a light water reactor causes the vessel to fail while there is still overpressure left in the reactor coolant system, the melt may be ejected in such a way that parts of it travel up in direction of the dome of the reactor containment. The melt flows through the breach, it is dispersed, a part of it may collect as a film on the adjacent walls, and parts of the film may be re-entrained into the main stream. The vapor blowing out of the breach oxidizes the metal components of corium. The reaction is exothermic and produces hydrogen which may burn downstream when mixing with oxygen of the containment atmosphere. At the Forschungszentrum Karlsruhe, the experimental program DISCO [1] was started to investigate, in a 1:18 scale, the thermal hydraulics of the dispersion processes. In order to take advantage of the extensive experimental experience in the United States, two experiments were performed with thermite as corium simulant in a 1:10 scale. The experiments were set up and performed at the Sandia National Laboratory (SNL) at Albuquerque. The report describes the analysis of the more energetic of the SNL experiments.

2 THE PHENOMENA DURING MELT DISPERSION

This chapter is intended to grossly outline the physical processes that play a role. **Fig. 1** shows an sketch of the reactor pressure vessel and the adjacent structures and an artist's view of the melt during dispersion. Note that this is the experimental mock-up of DISCO and not a sketch of the reactor.

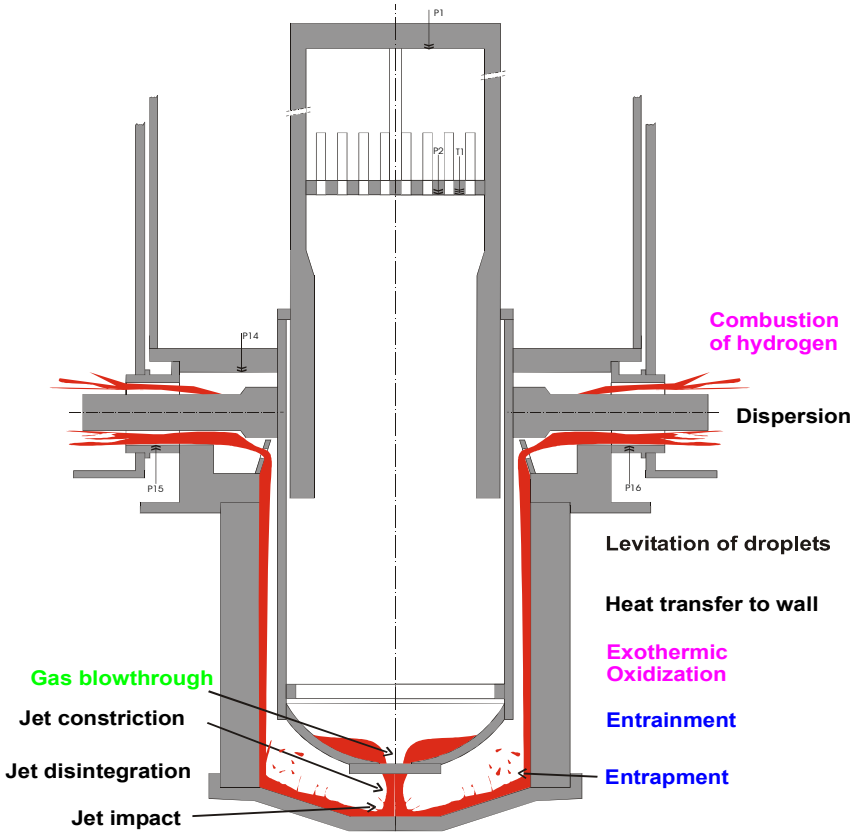

Fig. 1 Sketch of a model of a reactor with symmetric cavity and dominant phenomena

The reactor cavity into which the pressure vessel is placed forms a cylinder concentric to the vessel with openings to the reactor dome at the upper end of the annular section. The two gray structures extending horizontally outwards from the vessel are the main water pipes around which a gap is open to the adjacent compartments of the reactor building. The phenomena under investigation are listed close to the location where they occur.

The flow of melt to the outside of the pressure vessel is governed by the upstream and downstream conditions. During the DISCO-C (C=cold, the simulant material is water) program, and using code calculations, the phenomena leading to a gas blowthrough have been identified to play a role. The liquid melt first leaves the breach in an almost single-phase liquid flow. At a given low liquid level in the pressure vessel, the jet becomes two-phase in such a way that the center of the jet entrains vapor from the vessel. The change in flow regime has a substantial influence on the dispersion processes downstream.

Jets leaving pressure vessels at high velocities are subjected to a constriction of the jet diameter. The associated consequences on the mass flow need to be carefully modeled by the code. When leaving the breach, the jet may partly disintegrate due to the shear forces acting on it. Droplets leaving the jet may have different sizes than those being formed when the jet impinges on the cavity bottom. However, due to the lack of measurements, both processes are being addressed by the same droplet generation model.

Downstream of the impact area, a film of the liquid melt may be formed on the cavity bottom and the side walls. Droplets may be entrapped into the film. The rest of the droplets, especially those of a small size, may leave the cavity without contact to the cavity walls. The melt in the film exchanges heat with the colder walls. A part of the film may freeze and form a thin crust on the wall. If conditions are met, the vapor flow may entrain droplets out of the film. These droplets are generally small enough to be levitated by the vapor flow and are thus swept out of the cavity.

Beyond the top exit of the annular section of the cavity, the liquid film and the droplets meet a complicated structure with which they may interact. This part is not subject of the present investigation because in the SNL experiments, the annulus exit was straight up into the open reactor dome, see Fig. 3 of chapter 4. The dispersion has been achieved when the melt exits either the top of the annulus or the point where the water pipes join the open cavities of the reactor building.

While the melt flows through the cavity, its surface area to the adjacent vapor is largely increased. The steam which was either in the cavity before breach opening or is flowing out of the reactor pressure vessel after gas blowthrough reacts with the metal components of the melt. The reaction is exothermic and the products are oxides and hydrogen. Inside the cavity, there is not enough oxygen for hydrogen combustion. However, when hydrogen leaves the cavity, conditions are met in the reactor dome for a steady flame which adds reaction energy to the dome atmosphere.

These are the phenomena which have to be addressed in the recalculation of the experiments and when extrapolating to reactor conditions.

3 THE TRANSIENT FLUID DYNAMICS CODE

To accompany the ongoing experimental program, to identify physical phenomena of importance, and to extrapolate to reactor conditions, a CFD (Computational Fluid Dynamics) code is being used. The multiphase code chosen is AFDM (Advanced Fluid Dynamics Model [2]) of the SIMMER family of codes which has two dimensions and three velocity fields. This allows to track water, molten corium, and a gas-vapor mixture.

The code algorithm allows an easy addition of explicit models which address the physical phenomena of the melt dispersal, such as formation and entrainment of liquid films on the cavity walls, melt oxidation in the cavity, and hydrogen combustion in the reactor dome. These explicit models are superposed to the r-z-geometry of the Eulerian cell set of AFDM. There is no intention to resolve the velocity and mass concentration profiles expected in the given geometry. This would require cells of only millimeter size, and lead to inoperable cell numbers. Instead, there are only several hundred AFDM cells. This number is subject to change, especially because it governs numerical diffusion and smearing of distinct interfaces. This may have substantial influence on the way the dispersed melt may interact with the steam. Therefore, the report addresses question of discretization sensitivities.

3.1 THE MELT DISPERSION MODELS

By using predefined volumes consisting of clusters of Eulerian cells of AFDM, chemical reactions are evaluated for the representative mixture of reactants. While AFDM distinguishes only melt, water, steam, melt vapor, and noncondensable gas, the volumes of clusters may be filled with two different kinds of melt, oxide and metal, and three different kinds of noncondensable gas, nitrogen, oxygen, and hydrogen. **Table I** shows the components of both codes sections.

AFDM standard	Velocity field	Added model
structure	-	-
melt	**1**	oxide melt
melt particles	**1**	metal melt
water	**2**	-
melt vapor	**3**	steam
steam	**3**	nitrogen
noncondensable gas	**3**	oxygen
	3	hydrogen

Table I Components of the standard code and the added models

Besides the model sections added for the chemical reactions, a second model calculates the hydrodynamics in the vicinity of liquid corium films at the walls of the cavity outside of the reactor pressure vessel. The film model is specified for each Eulerian cell adjacent to the cavity walls. In cells adjacent to the outer walls of the cavity, a heat conduction model was implemented to calculate the potential formation of melt crusts.

3.2 CHEMICAL REACTIONS IN THE CAVITY

Chemical reactions between steam and the metal component of the liquid melt produces hydrogen and metal oxide. The present model does not treat reactions between melt and oxygen. The reaction is governed by the diffusion of steam through the gas boundary layer to the surface of the melt droplets. The steam diffusivity is

$$D_{H2O} = \frac{C_{dif}}{p} T_{film}^{2.33}$$

This is an empirical correlation with the temperature T_{film} of the gas film close to the droplet surface and the pressure. The correlation demands a coefficient C_{dif} the value of which depends on the material, here

$$C_{dif} = 4.4 \cdot 10^{-6} \frac{Pa \cdot m^2}{K^{2.33} \cdot s}$$

The Reynolds number of the melt droplets moving at Δv relative to the gas-vapor mixture is

$$\mathrm{Re} = \frac{\rho_{gas}\, d\, \Delta v}{\eta}$$

where η is the gas mixture dynamic viscosity as calculated by averaging over all AFDM cell values of the cavity. The nondimensional mass transfer coefficient, Sh, which is the product of the steam volume flow and the droplet diameter divided by the droplet surface area and C_{dif} is given by the empirical correlation

$$Sh = 2.6 \cdot \sqrt{\mathrm{Re}} \sqrt[3]{\eta \left(D_{H2O} \rho_{gas}\right)^{-1}}$$

Finally, the rate at which the reacting steam is transported to the droplet surface A is

$$\frac{d}{dt} m_{H2O} = -\frac{A}{d} Sh \cdot D_{H2O} \rho_{steam}$$

All steam transported to the surface is supposed to react instantaneously because the reaction velocities are large compared to the diffusion velocities. One mol of steam generates one mol of hydrogen. Among the values calculated by the model is the total amount of hydrogen generated in the cavity as a function of time.

3.3 FILM ENTRAPMENT AND ENTRAINMENT AT CAVITY WALLS

For each computational cell that lies adjacent to an outside cavity wall, models are added to the code to describe the formation of liquid films and the entrainment of droplets out of the liquid film. A liquid film is defined at the bottom horizontal section and the outer vertical section of the cavity wall. The film is supposed to have a negligible velocity. All three velocity fields of the code are already occupied, and a moving film would need a flow-regime dependent subdivision of given computational cells which are limited to use only cell-averaged values. The entrainment model is based on a modified Whalley-Hewitt correlation

which depends, among others, on the liquid film thickness, δ, which happens to be an input value to the correlation.

The entrainment rate, ε, of the modified Whalley-Hewitt correlation is

$$\varepsilon = C \cdot A \cdot \frac{\tau \cdot \eta_{gas}}{\sigma_{liq}} \cdot \frac{\rho_{gas}^2}{\rho_{liq}^2} \cdot \exp\left(-5 + 6.8 \tanh\left(6 \frac{\tau \cdot \delta}{\sigma_{liq}} \right) \right)$$

where C is a constant to be adjusted to fit experimental data, A is the film surface area, τ is the shear stress on the gas side of the film surface, η is the dynamic viscosity, and σ is the surface tension. To the original correlation has been added the ratio of the densities of gas and liquid, ρ_{gas}/ρ_{liq}, an addition which was found to be necessary to match water and thermite data at the same time. The exponential function is a tentative fit to a cluster of experimental points published in [3].

For the entrapment of droplets on the walls, a simple model of mass transfer rate is used which is proportional to the liquid droplet flow perpendicular to the wall. The entrapment rate is

$$\vartheta = C \cdot A \cdot v_{droplet}^{\perp} \cdot \overline{\rho} \cdot Ku^{-2}$$

where C is a constant, A is the surface area of the wall, $v^{\perp}$ is the velocity perpendicular to the wall, $\overline{\rho}$ is the liquid density per cell volume, and *Ku* is the Kutateladse number which is $\rho_{gas} v_{gas}^2 \; / \sqrt{g\sigma\left(\rho_{liq} - \rho_{gas}\right)}$ with the standard gravity *g*. From analyses of experimental results, see [4], the Kutateladse number was found to correlate with the fraction of liquid mass ejected out of the cavity if the velocity v_{gas} is the maximum value of the upward annular gas-vapor flow in the cavity. This led to the above formula so that at large *Ku*, the entrapment is reduced because the droplets are swept away by the gas-vapor flow.

As already criticized by [5], it is questionable whether the entrainment rate is proportional to the liquid viscosity as in the original formulation. Better results have been obtained by using a constant reference viscosity, or by the vapor viscosity as in the formula above. For low pressure corium dispersions, the shear stress may not be well represented by a formula with a two-phase friction multiplier established for annular flow in pipes. A smooth film surface shear stress has given better results.

The flow is highly transient, and the dimensions of the cavity are such that flow profiles cannot develop because of the abrupt changes of flow directions. Therefore, the steady state entrainment formula may not be fully valid. This shows also the need for adjusting the constants C in the entrainment and entrapment equations above. Local and transient measurements of flow and film parameters are difficult which limits the assessment of possible alternatives to standard entrainment models.

3.4 HEAT TRANSFER BETWEEN FILM AND WALL

If a liquid film of the dispersed melt is formed on the cavity walls, the heat transfer to the cold structures may lead to the formation of crusts which may have an influence on the mass being dispersed out of the cavity. Therefore, a heat transfer model was added to the code. The wall structure consists of concrete, as well in the experiment as in the prototype. A thermal wave can travel about 2 mm into the concrete of the experiment and about 6 mm into that of the prototype, given a total transient time of 5 s and 50 s, respectively. It is sufficient to divide the concrete wall into three concentric cylinder rings, the innermost of which represents the concrete wall surface. Therefore, this ring has a thickness of only 7% of the assumed thermal penetration depth, whereas the two following rings represent larger masses. Inside the concrete, heat is transferred by conduction at constant concrete conductivity. Between the concrete surface and the liquid film, a gap resistance can be specified. The film is supposed to be at uniform temperature. The energy balance takes into account the melting and freezing with a given constant fusion energy. The heat transfer from the film to the adjacent gas flow is calculated by the Dittus-Boelter correlation for the Nusselt number, Nu.

$$Nu = 0.023\,\mathrm{Re}^{0.8}\,\mathrm{Pr}^{0.4}$$

The Reynolds number, Re, is calculated for each cell with the available gas velocity. The velocity of the liquid film is assumed to be zero. The liquid of the film can only be transported downstream if it is first entrained, and then entrapped at a different location.

3.5 THE DISPERSED MELT FRACTIONS

The objective of the model of entrapment and entrainment of liquid films was to select equations with a single set of parameters which matches all experimental results, independent of the material combination used. The difficulty lies in the proper selection of the multipliers of the entrainment and entrapment correlations. An empirical approach for finding the proper parameters has been followed. Code results point towards a certain consistency of the present model equations when comparing calculated dispersion rates with those of the DISCO-C and SNL thermite experiments.

Fig. 2 shows the comparison of measured and calculated dispersion fractions. The fraction is defined by the ratio of the liquid mass collected downstream of the cavity exit to the total initial mass. The cavity exit is at the upper end of the vertical annulus. Any liquid beyond the annulus exit is supposed to be dispersed. The figure collects data of the DISCO-C experiments and the two Sandia thermite tests, SNL/Sup-1 and SNL/Sup-2. The DISCO-C (C for cold) experiments were run with water as corium simulant, and nitrogen as vapor simulant. Additional DISCO experiments with helium instead of nitrogen and wood's metal instead of water are also shown here (dashed curve in Fig. 2) although they would require different multipliers on the entrapment correlation to yield satisfactory results. At this stage of the analysis, the question whether only the entrapment rate is responsible for the lack of consistency of the dashed curve cannot be answered. It is quite possible that a model for the movement of liquid films on the cavity walls is needed. However, this model would have to be verified on transient data from experiments which are not available.

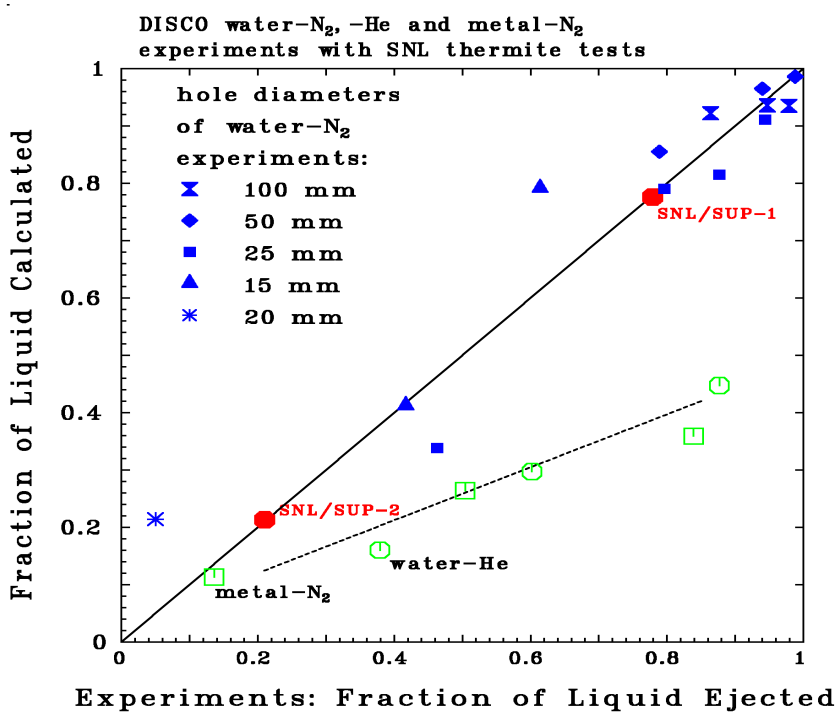

Fig. 2 Measured and calculated dispersion fractions of the DISCO-C and SNL-Sup programs

4 THE SNL/Sup-1 EXPERIMENT

From the two thermite experiments made at Sandia National Laboratory, documented in a Sandia report [6], the SNL/Sup-1 experiment has the larger breach area. Therefore, the transient is shorter and the chemical reactions are more violent and have a greater influence on the transient. Besides the geometric scaling, the reaction parameters of the melt simulant are expected to pose the greater difficulties when extrapolating to reactor conditions. This is the reason for choosing SNL/Sup-1 for the reference calculation. The experimental mockup is a 1:10 scale model of a reactor cavity concentric around the reactor pressure vessel with an opening to the reactor dome at the top of the annular section of the cavity. **Table II** shows a comparison of experimental and code geometries.

	experiment	**code**
distance breach-cavity bottom (m)	0.12	0.12
cavity height (m)	1.41	1.52
outer cavity radius below nozzles (m)	0.317	0.317
flow area at cavity exit (m^2)	0.168	0.172
flow area below nozzles (m^2)	0.0825	0.0833
horizontal nozzle flow area (m^2)	0.033	0.034
cavity free volume (m^3)	0.246	0.254
pipe inner radius (m)	0.0465	0.056
pipe volume (m^3)	-	0.032
crucible empty volume (m^3)	-	0.041
accumulator volume (m^3)	0.254	0.250
volume of accumulator+pipe+crucible (m^3)	0.307	0.323
containment free volume (m^3)	99.	97.6

Table II Dimensions of the experimental mock-up and the code

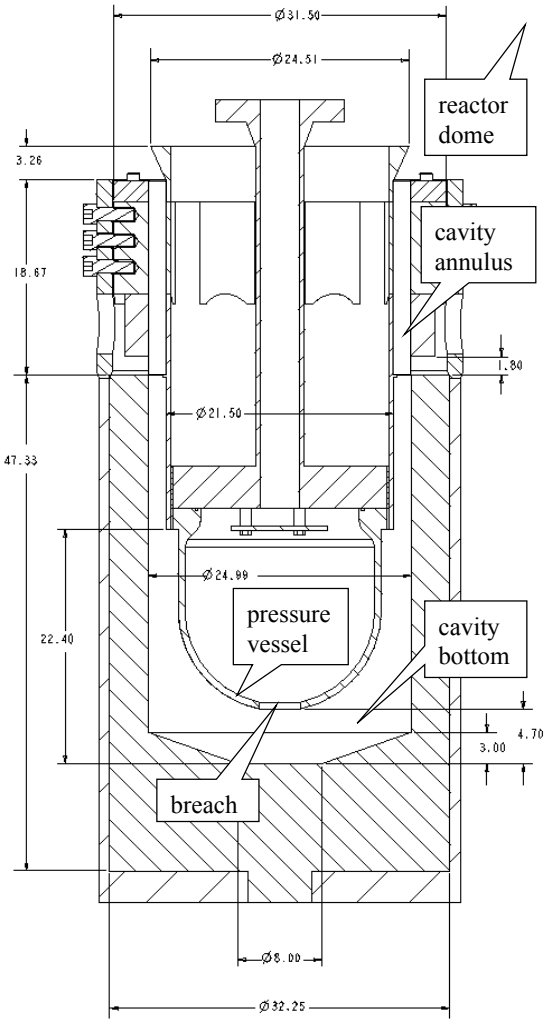

Fig. 3 Sketch of the SNL experiment, measures in inches

Fig. 3 shows a sketch of the lower part of the SNL-Sup experiment.

4.1 THE INITIAL AND BOUNDARY CONDITIONS

In the lower head of the pressure vessel, 62 kg of thermite at 2500 K, initially collected in the "crucible", are discharged through a concentric breach of 0.1 m diameter. Above the molten thermite, the "accumulator" which represents the free volume of the pressure vessel has a volume of 0.254 m^3. The accumulator and the pipe that connects it to the crucible are filled with steam and nitrogen at a total pressure of 1.106 MPa.

The flow through the breach must be carefully modeled to yield the proper thermite exit velocities. The staggered grid of the Eulerian code demands that the breach be at least two cells long. The breach is one cell wide. To model the jet constriction, the upper breach cell must have a smaller diameter. If the jet would exit into a volume without a close-by cavity bottom, the exit velocity, v_{ex}, would simply be $v_{ex} = \sqrt{2\Delta p / \rho}$ where Δp is the pressure difference across the breach and ρ=3880 kg/m^3 the liquid thermite density. For SNL/Sup-1, the driving pressure difference is $0.9 \cdot 10^6$ Pa, and the velocity becomes 22 m/s.

Fig. 4 shows the calculated thermite velocity together with the jet liquid volume fraction just below the breach.

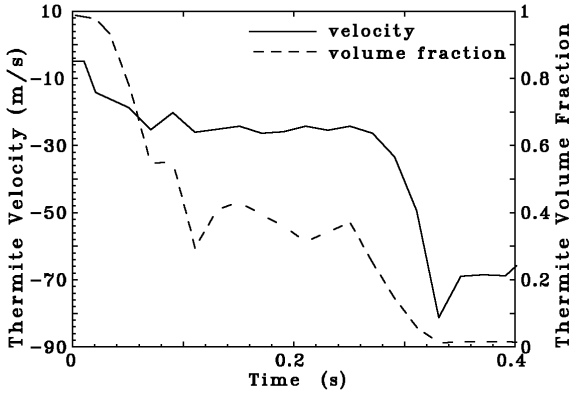

Fig. 4 Calculated conditions at the exit of the pressure vessel

The jet starts off almost single phase. Liquid volume fractions fall to 55% at 0.07 s and the jet becomes two-phase. At this time, the jet has been accelerated to 25 m/s. The subsequent two-phase jet velocity stays around 26 m/s. After 0.3 s, there is little liquid left to be entrained into the vapor jet, and velocities grow to about 70 m/s. The mass flux out of the crucible is shown in **Fig. 5** together with the thermite inventory of the crucible.

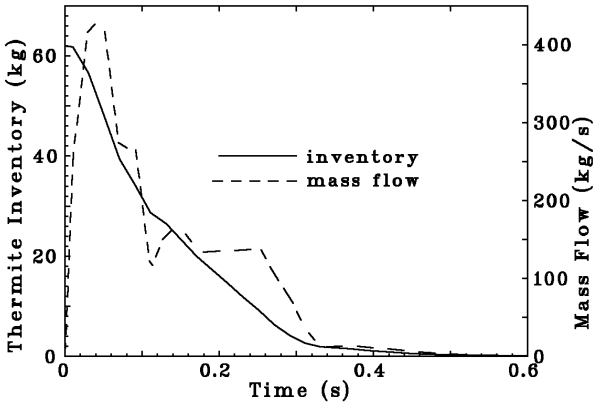

Fig. 5 Melt inventory of the pressure vessel and exit mass flow

If the breach was sharp-edged and the liquid velocity was zero in the crucible, the steady state mass flux, m_{ex}, would be $m_{ex} = v_{ex} A \rho C_1 C_2$ where A=7.854·10^{-3}m^2 is the breach area, C_1=0.6 is the jet constriction ratio, and C_2=0.99 is the velocity profile factor. This yields m_{ex}=400 kg/s. The figure shows a maximum mass flux of 430 kg/s between 0.02 and 0.06 s. The flux sharply decreases when the jet becomes two-phase.

The measurements with the highest time resolution are those of the pressures. The first objective of the recalculation is therefore to match measured pressures. The results are already shown here to discuss the difficulties to recalculate the conditions inside the pressure vessel which are the driving conditions for the melt dispersion. The second objective is to match integral results such as the total thermite mass dispersed out of the cavity and the total amount of hydrogen produced.

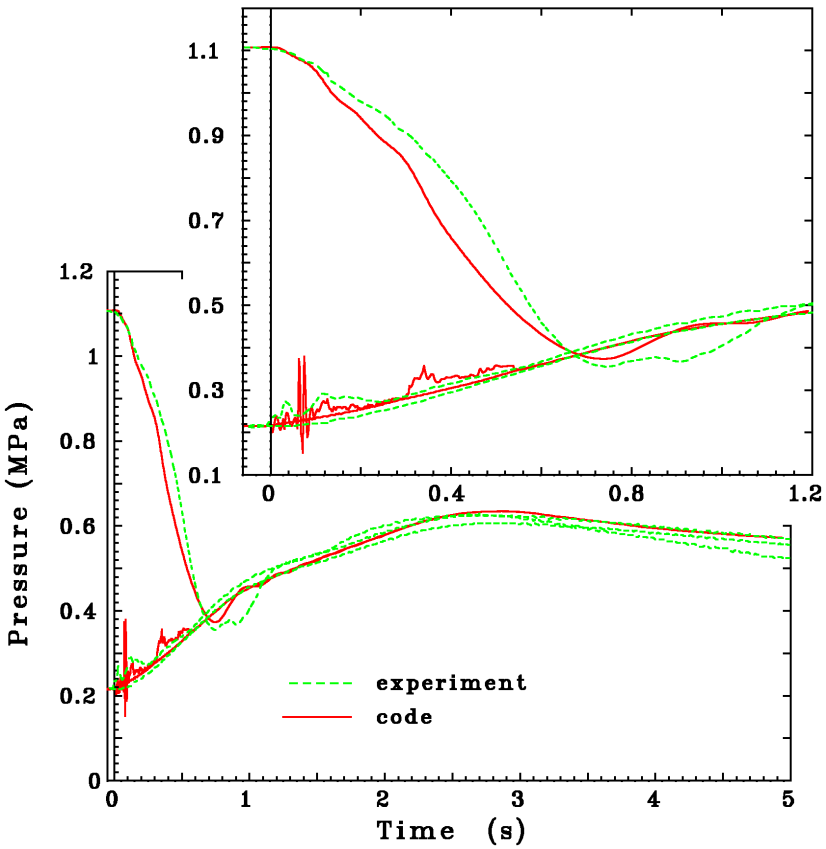

Fig. 6 Measured and calculated pressures of the SNL/Sup-1experiment

Fig. 6 shows the pressure transients of the experiment (dotted lines) and the code (solid lines). The uppermost pressure is that of the accumulator inside the pressure vessel. Code pressures match well with measurements until 0.2 s, see upper part of the figure for the early transient, then the code yields lower vessel pressures. At 0.7 s, both curves cross, and the experiment shows a substantial pressure undershoot thereafter which is much smaller in the calculation. The pressure curves below are those for the cavity bottom. Both curves show oscillation with those of the code more pronounced. Pressures in the cavity and the dome

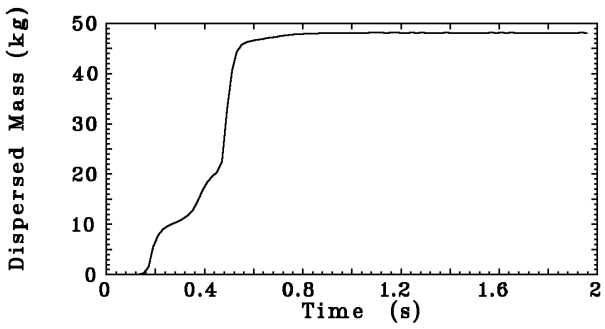

Fig. 7 Calculated dispersed thermite mass of the SNL/Sup-1experiment

start at about 0.22 MPa. The pressures of the cavity are higher and show small maxima because of thermal and chemical interactions. The pressure peak after 0.1s is lower for the code, but the general course looks similar and comes at the proper time. Experimental cavity pressures stay 0.025 MPa above dome pressures, while the code calculates a second peak in the cavity at 0.35 s with subsequent pressures well matched. **Fig. 7** shows the thermite mass collected downstream of the cavity as a function of time. The code calculates that 48.1

kg of thermite are dispersed out of the pressure vessel and cavity while the experiment yielded 48.3 kg which is the fraction dispersed from the cavity (=0.779), see Table 14 of [6],

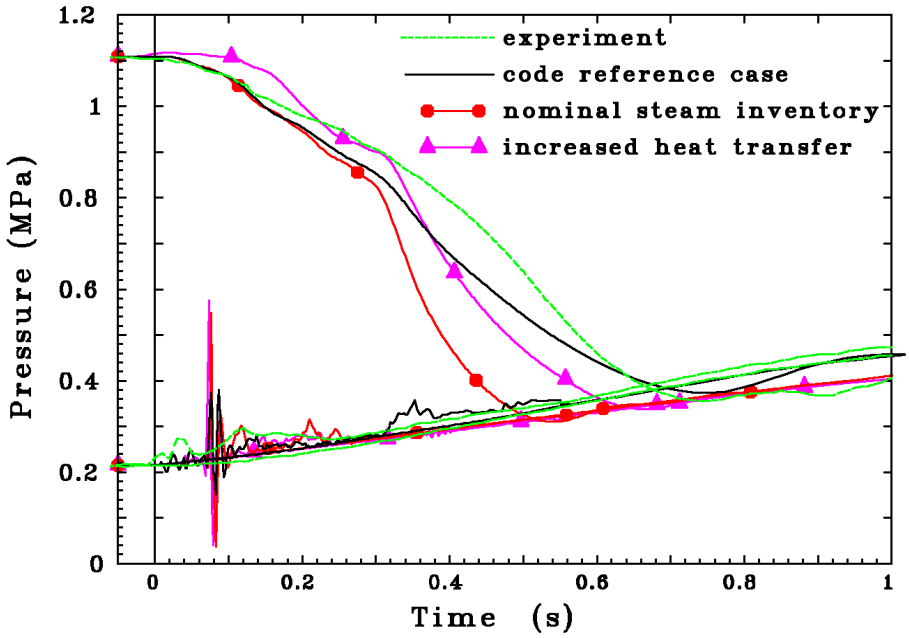

Fig. 8 Measured and calculated pressures for the vessel steam inventory study

multiplied by the initial mass of 62 kg. The code calculates “ideal” conditions and does not take into account the molten mass of the brass plug and the crucible wall.

There are initially 74 mol of steam in the pressure vessel of the experiment and the code. If this was the only steam in the pressure vessel, the vessel pressures would decrease much faster in the calculation than they do in the experiment, and cavity pressures would be lower. **Fig. 8** shows the early pressure histories of several code runs. First, a case with the nominal (small) steam inventory in the accumulator yielded good pressures for the first 0.3 s, but then a rapid decrease which was not found in the experiment. Second, with the nominal steam inventory, the heat transfer to the hot structures of the crucible was increased resulting in early overpressures, reasonable pressure levels until 0.33 s, and then again a pressure decrease below experimental levels. At the same time, pressures in the cavity were higher in the experiment indicating that there were sources of energy not taken into account in the calculation. Additionally, the melt mass dispersed out of the cavity was much lower than in the experiment. Finally, the reference case of Fig. 6 is shown where water is added to the accumulator of the calculation which yielded a net evaporation of about 2.5 kg equivalent to 139 mol of steam. This added mass cannot be explained by the unintentional reopening of the valve that fed vapor into the accumulator of the experiment, as reported in [6]. In the experiment, vessel and cavity pressures equilibrate at 0.7 s. During these 0.7 s, this would only add 2.4 mol of steam. Another source of water could potentially be steam which had condensed prior to the transient. However, this could not have been more than about a few 10 mol. Because the code results with the added water gives, by a large margin, the best results, especially for the cavity pressures at times later than 0.4 s, the associated initial conditions have been chosen as reference. However, the reason why pressures in the vessel are that high between 0.3 and 0.6 s cannot be explained by the calculations. There may be a lack of adequate models for in-vessel steam interacting with hot thermite. Because cavity pressures are well matched at the same time one could argue that water in the concrete wall

may have been gradually released to raise cavity pressures. Roughly 100 mol of water would have to be drawn from the walls. The cavity surface area is 3.1 m^2. During the first Δt=0.7 s, the thermal wave travels a distance of $\sqrt{a\Delta t} = 0.7mm$ if the thermal diffusivity of concrete is $7 \cdot 10^{-7} m^2/s$. Therefore, a concrete volume of $2.2 \cdot 10^{-3} m^3$ may be affected corresponding to 4.4 kg. Eventually, 40 mass percent of water would have to be stored in the concrete walls which is not quite conceivable. Therefore, it cannot be demonstrated that all water necessary for good pressure recalculations can be associated to a physical process identified at this stage of the analysis.

Outside the pressure vessel, in the cavity and the containment volume of 99 m^3, there are initially 6308 mol of a mixture of air, steam, and hydrogen at a total pressure of 0.213 MPa. The mol fractions are 51.4 % for air, 45.2 % for steam, and 3.3 % for hydrogen. The breach in the middle of the lower head of the RPV is closed by a plug. The plug starts to open at 0.0 s. In the calculation, the time interval to open the plug is set to 6 ms.

The amount of hydrogen that the code calculates to be generated in the cavity is 0.44 kg. The posttest gas analyses showed that 0.89 kg (442 mol) of hydrogen must have been generated. The experimentalists also give an explanation for this large value [6]. They argue that due to the noncoherence of the melt and steam during the dispersal (in the cavity, melt and steam are not in intimate contact all the time) part of the hydrogen may have been generated when the thermite droplets interacted with the atmospheric steam outside the cavity. Therefore, a specific model was added for the only purpose to add, beginning with the time the experiment reports the droplets to hit the top of the reactor dome (t=1 s), a hydrogen generation rate equivalent to half of the combustion rate which is an input parameter. At a time when the experiment reports that the droplets stop falling onto the operating deck (t=2.2 s), the hydrogen generation is linearly being reduced to zero. The total amount of 442 mol hydrogen is generated at t=3.3 s. This model has only been used for the recalculation of the SNL/Sup-1 experiment. It gives the best pressures at late times and confirms the hypothesis

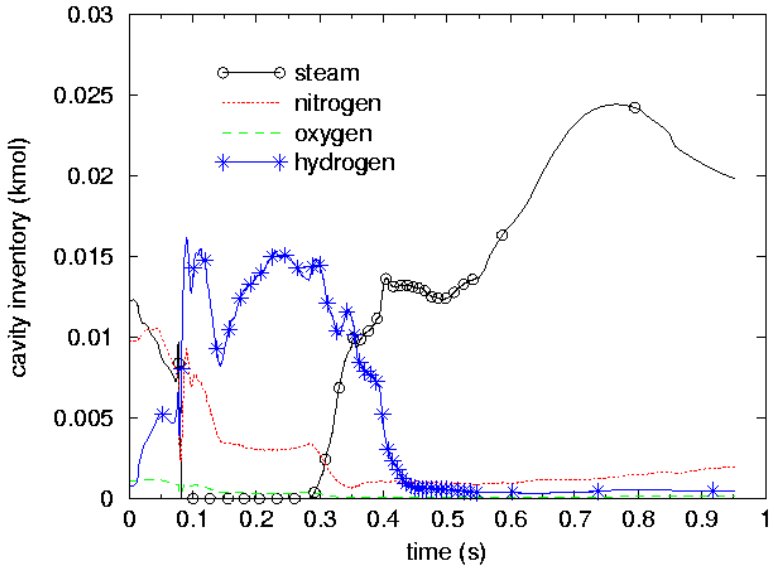

Fig. 9 Calculated cavity inventory for the experiment

of ex-cavity hydrogen generation.

The combustion rate depends on the conditions of the hydrogen jet that leaves the annular gap of the cavity into the open space of the reactor dome. The experimentalists report that a stable standing flame was visible. **Fig. 9** shows among others the hydrogen inventory in the cavity. Between 0.13 and 0.45 s, the code calculates that the jet contains about 80 mol% of hydrogen. The hydrogen jet velocities should be close to those calculated for the exit of the cavity. They are shown in **Fig. 10**.

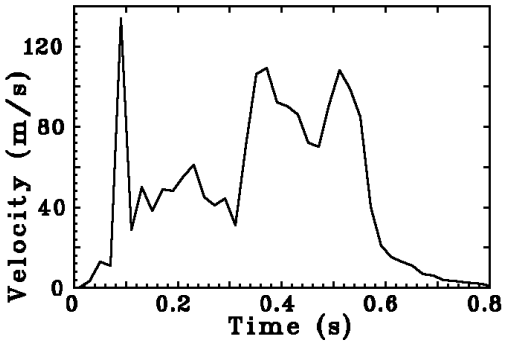

Fig. 10 Calculated cavity exit velocity

Velocities must be smaller than about 200 m/s to guarantee a stable flame which is the case. The width of the cavity exit is D=0.1 m. Using an average exit velocity of v_{fl}=70 m/s, the Froude number, Fr, is Fr= v_{fl}^2/(gD) and has a value of 5000. With this Froude number and according to [7], the flame should be 7.7 m long and thus extend to the upper part of the SNL dome model. The annular flame surface would thus be 31 m^2. The code model needs an input condition for the total combustion in the dome. This value is assumed to be a constant and has a dominant influence on the early pressure ramp in the dome and the cavity. The best results were obtained with a value of 0.4 kg/s which corresponds to a specific rate of 0.013 kg H_2/(m^2s). In the experiment, 3.3 mol% of hydrogen are reported to be added to the cavity and dome prior to the transient. Both volumes contain 6300 mol of gases. Therefore, the code initial hydrogen contents in the reactor dome is 0.41 kg. Because the code cannot distinguish between hydrogen which was generated during the transient and which was already there before, the combustion of 0.41 kg of hydrogen fully contributes to the energy release. In other words, it takes about a second to burn all pre-existing hydrogen at the rate selected for the present calculations. According to Fig. 17 which will be explained in the next chapter, the code calculates an end of the combustion at around 3 s. This does not comply with experimental findings where the standing flame has been observed until 7 to 8 s [6]. This would also require that hydrogen is generated for a longer period than the code assumes. To explain the discrepancy, the cavity code models would have to be changed so that hydrogen generation on thermite films would prevail longer and have a larger influence. This would touch basic assumptions of the present calculations. Experimental and code findings can be made consistent with the argument that the experimental observation cannot distinguish between an early flame at high energy release and a late flame without much gas supply from the cavity which would thus be very little energetic. Radiation from the hot gases to the dome structures is taken into account by a heat flux proportional to the temperature difference to an assumed structure mass of 19200 kg at an initial temperature of 270 K.

4.2 THE TRANSIENT AFTER BREACH OPENING

After breach opening, the melt is discharged into the cavity which has a volume of 0.254 m^3 (0.246 m^3 in the experiment, see Table II, page 7). From the analyses of the DISCO-C experiments, see [8], a rough picture of dominant processes has evolved. The picture is that there are two modes of flow through the breach. First, the melt leaves the breach as single phase flow. The single phase liquid jet disintegrates into a swarm of droplets. Among the code models to assess the droplet size, only the one has an influence that is governed by the Weber number. The droplet diameter is thus proportional to the surface tension of the liquid and indirectly proportional to the square of the velocity difference between droplets and the continuous gas field. The code calculations showed that it was necessary to define different critical Weber numbers for the vicinity of the breach and the rest of the cavity. Near the breach, shear forces may form droplets from the liquid jet and may split droplets already sheared off. The liquid jet may impinge on the bottom cavity wall and droplets may emerge when the liquid bounces back into the cavity. The critical Weber number needs to be smaller. For thermite, the factor on the nominal Weber number for droplets in an infinite gas stream is chosen to be 0.07. This value is lower than for the liquid water jet of the DISCO-C experiments. It may be argued that although thermite produced in the crucible has had a reasonable time to settle and vent off it is still filled with residual small bubbles which will grow during the discharge and thus increase the disintegration of the jet. Near liquid films on the cavity walls where droplets which emerge from film crests may be split in the main vapor stream, the critical Weber number is supposed to have values a little bit smaller (presently a factor of 0.4) than the standard value.

The thermite leaving the breach has a temperature of about 2500 K. All water that might have gathered at the cavity bottom and was not drained before the transient will be evaporated and driven out before t=0.09 s. The amount of puddle water was changed and found to have little or no influence on the dispersion. In the present reference calculation 0.18 kg of puddle water has been used.

The distance the droplets can travel depends on the driving pressure and the inertia of the droplets, and hence on the velocity of the jet. The code calculates a radial thermite velocity in the lower cavity of about 10 m/s. At 0.05 s, i.e. 0.044 s after complete breach opening, the melt has progressed to the outer periphery of the cavity which is at a radius of 0.31 m.

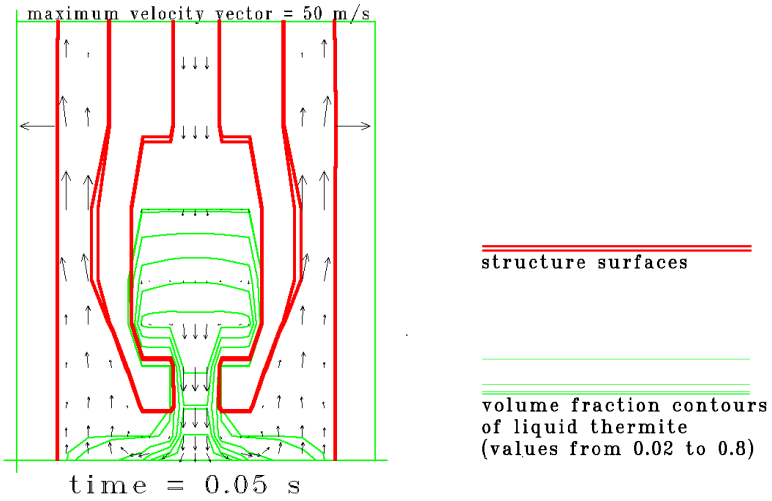

Fig. 11 Calculated melt contours and velocity vectors close to the breach

Fig. 11 shows the contours of thermite volume fractions. It gives a qualitative picture of the jet leaving the breach and the radial expansion at the cavity bottom. A substantial part of the droplets has been entrapped on the cavity walls and forms a liquid film. The two radial velocity vectors shown inside the upper outer cavity walls represent the by-pass flow through the horizontal nozzle.

The single phase jet soon becomes two phase because the pool inside the pressure vessel becomes so shallow that a gas-vapor blowthrough occurs at the breach, see [8]. The code calculates the time for gas blowthrough at 0.06 s. From now on, the liquid thermite in the lower cavity is accelerated to velocities beyond 30 m/s, see Fig. 4, page 9. The gas-vapor mixture may entrain droplets out of the liquid film and carry them out of the cavity. This is the first dispersion process. For the second process, the spray of droplets which has been and is being formed just downstream of the breach is carried away by the gas-vapor flow all the way through the cavity without touching the walls. This is the bulk process just after gas blowthrough.

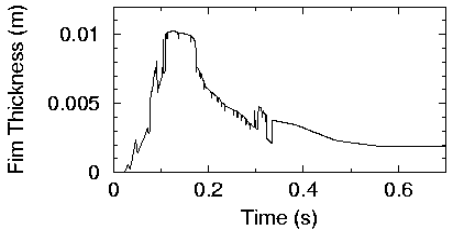

Fig. 12 Calculated average thermite film thickness in the cavity

The liquid thermite film produced by entrapment of droplets on the cavity walls rises quickly just after breach opening, see the film thickness averaged over all cavity wall cells in **Fig. 12**. The film builds up to a maximum thickness after 0.1 s, and then decreases quickly because of entrainment by the violent gas-vapor flow through the cavity. The final film thickness corresponds to 13 kg of thermite. The entrainment is proportional to the shear stress on the gas side of the film, and hence a function of the local tangential velocity vector. **Fig. 13** shows the vapor temperature and velocity averaged over the whole cavity which gives an indication of the flow conditions.

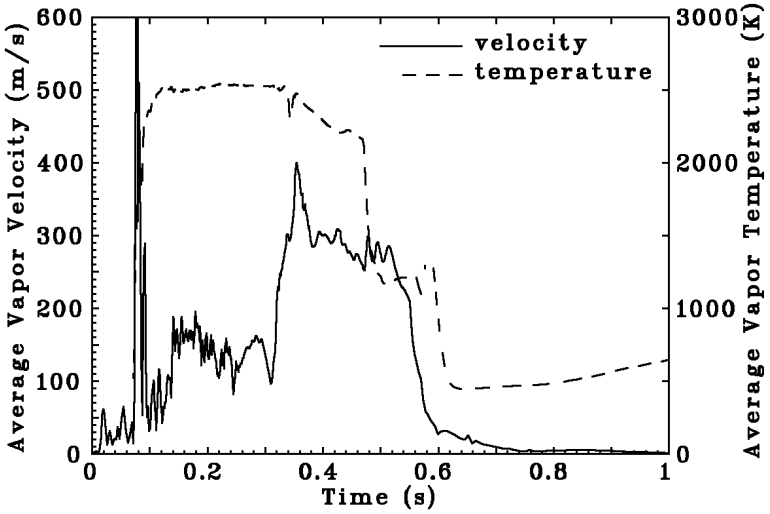

Fig. 13 Calculated average vapor temperatures and vapor velocities in the cavity

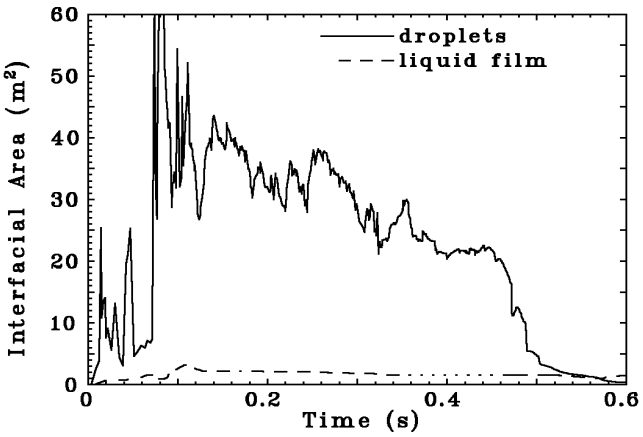

Fig. 14 Calculated total interfacial areas of droplets and liquid film in the cavity

After gas blowthrough, the vapor enters the cavity filled with thermite the interfacial area of which influences the heat flow from thermite to vapor. **Fig. 14** shows the total surface area between vapor and liquid thermite of the cavity. It initially grows to about 10 m^2 which indicates the development of smaller droplets. Note that the cavity outer walls have a total surface of 3 m^2. At 0.079 s, surface areas increase rapidly. The hot thermite heats up the vapor to temperatures around 2500 K. The vapor expands and the velocities increase. Peak velocities are over 600 m/s. This event may partly be produced by autocatalytic phenomena described in chapter 4.3, page 19, which depend on the averaging processes of the Eulerian grid and the associated numerical problems. The event is followed by a time interval of 0.2 s with surface areas around 35 m^2 and velocities between 100 m/s and 200 m/s. At 0.11 s, the total cavity surface is covered with a liquid film. After 0.3 s when the two-phase flow through the breach fades out and only vapor leaves the pressure vessel, average vapor velocities grow to 300 m/s.

The swarm of thermite droplets starts to exit the upper end of the cavity annulus just after 0.1 s. The code calculates that already 18 % of the inventory has left the cavity at 0.3 s, see Fig. 7, page 10. The dispersion ends around 0.7 s. With the droplets, vapor and gas is ejected

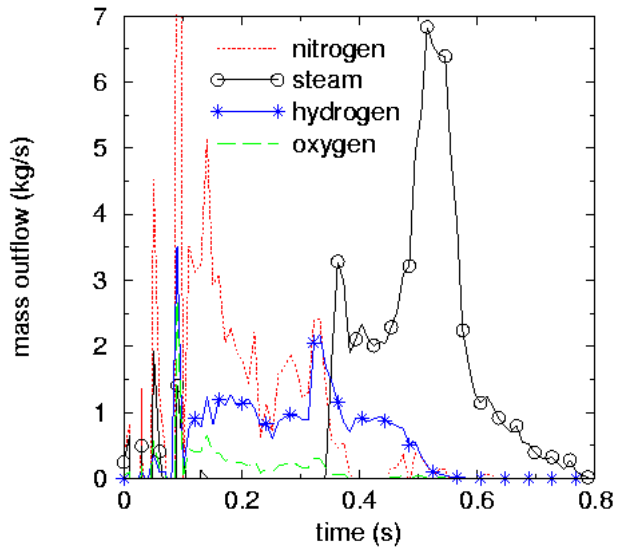

Fig. 15 Calculated mass flows out of the cavity into the reactor dome

into the reactor dome. It was not the objective to calculate in detail the subsequent mixing and chemical reactions of the gases in the dome. As described in chapter 4.1, the combustion is set constant. If combustion was to be calculated with appropriate tools, the outflow conditions at the cavity exit need to be known. **Fig. 15** shows the mass flows into the reactor dome for the period of dispersion. The hydrogen mass flow falls down close to zero at 0.55 s.

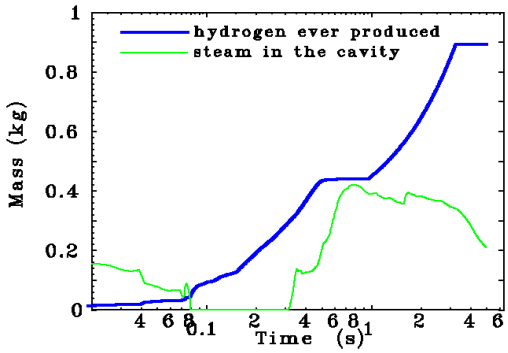

Fig. 16 Calculated steam inventory in the cavity and hydrogen mass

When the droplets in the cavity come into contact with the steam placed into the cavity prior to the test and the steam flowing out of the RPV, the metal component oxidizes and hydrogen is produced. **Fig. 16** shows the total hydrogen mass ever produced and the steam inventory of the cavity. Up to 0.04 s, there is little hydrogen production because the droplets do not penetrate a long distance, the relative velocities between droplets and steam are low, and because the droplet front practically pushes the vapor downstream. Only 20 % of the steam in the cavity reacts with the droplets. After gas blowthrough at 0.05 s, more steam enters the cavity with the melt. However, up to 0.08 s, the steam inventory in the cavity decreases because more steam reacts than enters from the pressure vessel. Between 0.08 and 0.3 s, the reaction is severely steam limited as already stated in [6], and all the steam entering the cavity reacts with the thermite droplets. After 0.3 s, the steam inventory increases and hydrogen production continues until 0.5 s. This is the time of intermediate hydrogen mass of 0.44 kg already mentioned in Chapter 4.1. The special hydrogen production model of the reactor dome, see last chapter, yields the additional hydrogen ramp after t=1 s.

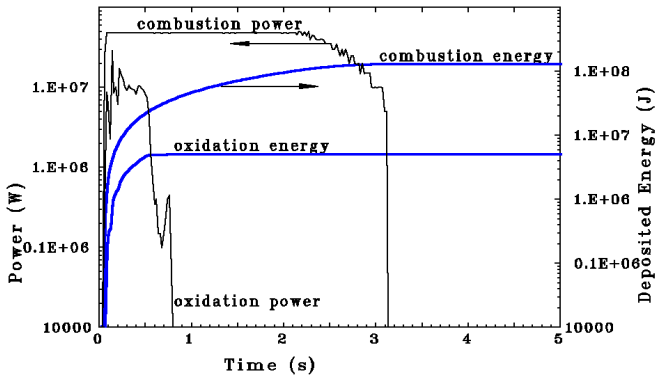

Fig. 17 Calculated power and energy of metal oxidation and hydrogen combustion

Fig. 17 shows the oxidation power released in the cavity, the combustion power in the reactor dome, and the accumulated energies. The total oxidation energy can possibly be

0.016 MJ/mol which is the specific value of thermite, see [6], multiplied by 897.7 mol thermite which yields 14.4 MJ. The maximum energy calculated to be produced in the cavity is 4.9 MJ which is 34% of 14.4 MJ. The power is released during the first 0.8 s. However, as stated in the last chapter, more oxidation is taking place later in the dome until 0.89 kg hydrogen are produced. This would raise the oxidation energy to 9.9 MJ while oxidation in the cavity alone yields only 4.9 MJ. With 127 MJ the combustion adds by far the larger part of energy. The combustion power is constant at 48 MW as a consequence of the constant combustion rate which is an input parameter, see last chapter. The power curve also shows how the combustion fades out according to the specific model added to the code.

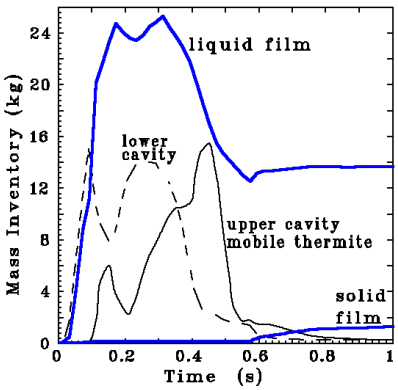

Fig. 18 Calculated cavity inventory of liquid and frozen films and mobile thermite

The liquid thermite film may freeze on the walls of the cavity. The code model only takes into account the bottom and outer side walls. **Fig. 18** shows the film masses in the cavity compared to the masses of mobile thermite over time. The heavy lines represent the films. A total of 90 g of thermite freezes on the wall very early during the transient. If this mass was evenly distributed over the whole outer wall surface the crust would be about 0.01 mm thick. The crust mass increases only after 0.57 s to yield a final mass of 1.3 kg. The liquid film stuck at the walls after pressure equilibration has a mass of 14 kg. The figure also shows how the mobile thermite is redistributed from the lower cavity into the upper cavity before it is ejected beyond the cavity exit. Note that the thermite that is trapped on the walls is no longer able to move by gravity or shear forces, but it can be entrained into the field of mobile thermite. **Fig. 19** shows the temperature distribution in the liquid film and the three wall cells at the cavity bottom at a radius of 0.25 m.

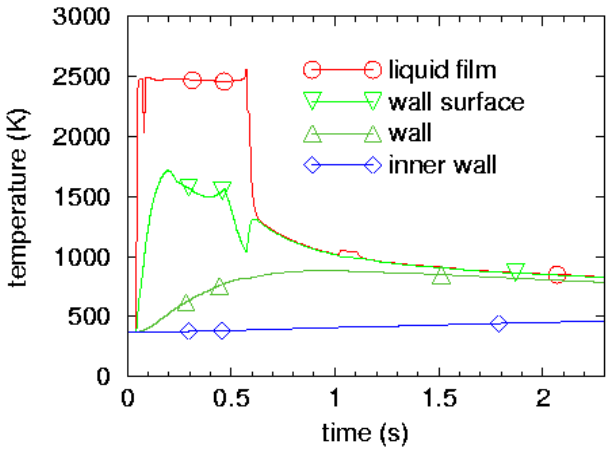

Fig. 19 Film and wall temperatures at a selected location of the cavity bottom

The top temperature is that of the film. It is close to the initial thermite temperature. The wall surface temperature grows to a maximum of 1700 K which is below the solidus temperature of thermite so that a thin crust is formed. After 0.55 s, the liquid film is totally entrained and the liquid blown downstream. The film temperature drops sharply. The residual crust thickness averaged over the cavity is calculated to be 0.02 mm.

4.3 THE CHOICE OF THE MESH SIZE AND THE TIME STEP SIZE

As already stated above, the Eulerian mesh is chosen without respecting the necessity to resolve concentration and velocity profiles. These profiles can neither be resolved by experimental methods, especially not for these fast transients. Liquid film profiles of the dispersed melt would need to be resolved as well, but only lumped parameter models are presently available for entrainment and entrapment correlations. The choice of the mesh is therefore guided by limiting calculational expenditure by reducing the number of cells.

The transient is characterized, among others, by the thermal and chemical interaction between the hot melt and the relatively cold steam. Although the code uses higher order differencing, the smearing of interfaces and mass fronts plays a role. If, for example, the cell size is large, the progressing melt may enter a front cell in large quantities, and will instantaneously be mixed with the other components present in that cell. The calculation of the intracell exchanges follows. The chemical reaction and the heat up of steam may enhance velocities and mixing so that this is quite the contrary to a self-limiting process. However, the exothermic energy is calculated for the whole ensemble of liquid droplets in the cavity, and is then distributed over all the melt. This prevents local energy peaks. The code uses a time factorization method to allow easy access to constitutive equations. However, this method has been criticized that the feedback from intracell exchanges will not occur at the present time step. This increases difficulties at sharp interfaces. To resolve these problems, the physics at the interfaces would need to be described and appropriate models introduced into the code. The lack of insight into these highly transient phenomena and the lack of models demands for a parametric approach.

For recalculations of experiments, it is possible to find a set of cells sizes and time step sizes for which calculated values correspond well to measured ones. However, when extrapolating to the prototype, there is no longer any experimental confirmation. Therefore, a study of sensitivities needs to define the uncertainties, both in experimental and prototypic geometry. The study has been performed with an early input data set which is different to the reference calculations. Three mesh cell sets have been investigated, the coarsest of which has 14 x 16 cells and has been used extensively because of fast running times. The code solves the conservation equations with a fractional step method. The time step size must therefore be limited by a material Courant number. This implies that the time step must not be longer than the time needed for a given mass to traverse a given cell. Usually, half of this time is used as a limit which corresponds to a Courant number of 0.5.

Table III shows the dispersed melt fraction in the last column. The second line gives the experimental value with which calculations will be compared. However, the recalculations have been evaluated primarily on how close calculated pressures came to experimental results. This is because the pressures resolve well the transient, and because they show

directly how reactive the thermal interactions are inside the cavity. **Fig. 20** shows the pressures of the cases A, B, C which are listed in Table III in the section just below the experiment. These recalculations in all three mesh sets on experimental scale have optimized Courant numbers so that pressures correspond best with the experimental reference.

	scale	mesh set (smallest length (m))		Courant number	fraction of melt dispersed (%)
experiment	**1:10**				**77**
Case A	**1:10**	14 x 16	(0.045)	Middle	76
Case B	**1:10**	19 x 22	(0.023)	Low	66
Case C	**1:10**	30 x 36	(0.012)	Low	42
Case D	**1:1**	14 x 16	(0.45)	*Very Low*	*74*
Case E	**1:1**	14 x 16	(0.45)	*Middle*	*86*
Case F	**1:1**	14 x 16	(0.45)	*High*	*99*

Table III Variation of cell size and Courant number*

*)The numbers are: very low = 0.05 to 0.07, low = 0.11 to 0.15, middle = 0.25 to 0.3, high = 0.6

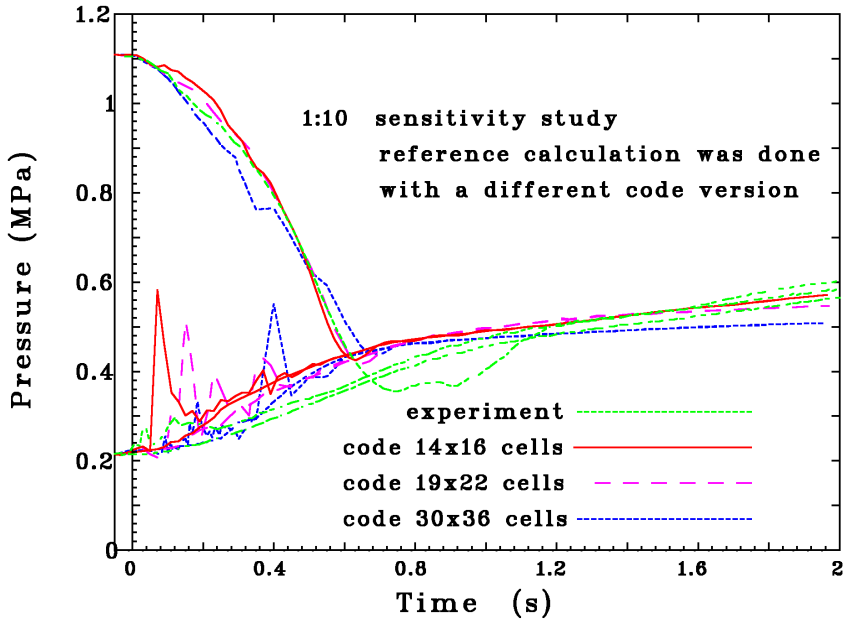

Fig. 20 Calculated pressures of the sensitivity study, reference pressures see Fig.6

The pressure history of Fig. 20 is taken at three locations, the reactor pressure vessel, the cavity, and the reactor dome. The pressure of the reactor pressure vessel starts at 1.1 MPa. All vessel pressures fall consistently until they reach cavity pressures at 0.7 s. The cavity pressures are represented by the curves starting at 0.2 MPa and having pressure spikes. They show that the coarsest mesh set (14x16 cells) yields the earliest spikes. As the mesh set becomes finer, the spikes occur later and the early cavity and vessel pressure history correspond better with the measured one. A coarser mesh favors an earlier mixing of melt with the gas-vapor mixture of the lower cavity. At 0.1 s, when the melt has progressed radially to the outer periphery of the cavity bottom, the coarsest grid yields a droplet swarm thickness almost three times as large as for the finest grid so that the front of the droplets covers a larger gas-vapor volume. The smaller the cell size, the smaller the fraction of melt

ejected out of the cavity. For the very fine mesh set, the part of the melt that is entrapped as a film on the cavity walls, is limited by the cell size adjacent to the wall. For numerical reasons, the film fraction in the cell is limited to 80%.

For the prototypic scale 1:1, the variation of the dispersed mass with the Courant number is shown in Table III, cases D, E, and F, which are three cases of the coarse mesh set, 14 x 16. These cases were run with three different Courant numbers, where a low Courant number means small time steps. **Fig. 21** shows the three time step sizes over the total extent of the transient. The main dispersion takes place between 0.5 s and 5 s. During this time, the very low Courant number yields a time step of about $7 \cdot 10^{-5}$ s, the middle Courant number $3 \cdot 10^{-4}$ s, and the high $6 \cdot 10^{-4}$ s. The middle and very low Courant numbers yield the ejected melt fractions closest to that of the experiment. Taking into account basic scaling considerations, the dispersed mass fraction should scale 1:1. The reasons for this are given in the chapter 5.2, page 26.

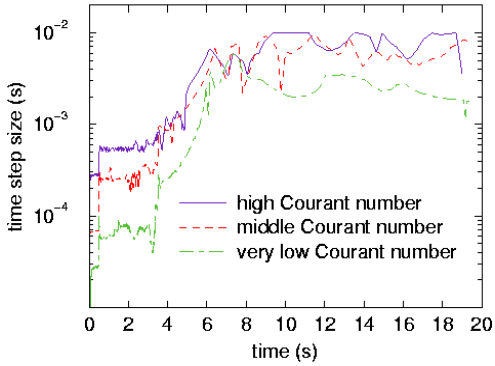

Fig. 21 Time step sizes of the code for the sensitivity study

The experiment was set up so that pressures would scale 1:1 with respect to prototypic geometry, see chapter 5.1. Therefore, pressures for the 1:1 cases can directly be compared to those of the experiment if the time scale is transformed by a factor of 10. **Fig. 22** shows this comparison for the cases D, E, F of Table III. Note that this is not the reference calculation which will be presented in chapter 5.1. The time scale at the top abscissa is that of the prototype. The bottom abscissa shows the time scale of the experiment. As will be

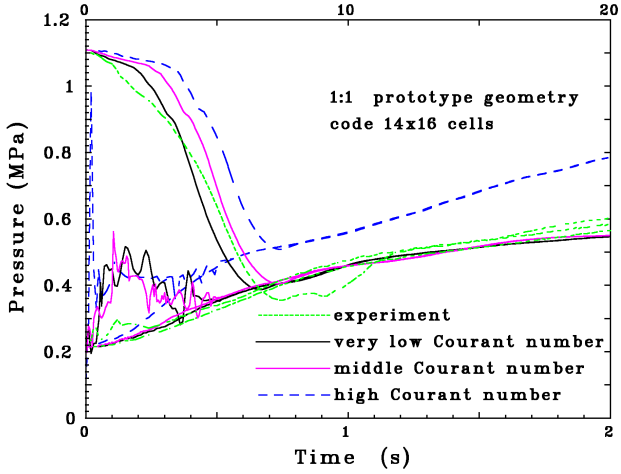

Fig. 22 Pressures of the sensitivity study in 1:1 scale, experiment in 1:10 scale

explained later, the droplet size is different by a factor of 1.7 between both scales. For the present large prototypic mass (there are 62000 kg of thermite in the pressure vessel), the large surface of the droplet swarm yields high cavity pressures early during the transient.

The very low Courant number yields the best pressures, but the middle Courant number yields reasonable pressures as well as reasonable dispersed mass. The largest deviations of dispersed melt fractions are +30% and –45% from the experimental value, see last column of Table III. The high Courant number produces very high pressure spikes in the cavity just after the breach opening, it delays pressure vessel depressurization and far too high cavity and dome pressures at late times. Due to the enhanced dynamics, the dispersed mass increases as well.

The sensitivity analysis has shown that the coarsest mesh set and a medium Courant number yields reasonable results, both in 1:10 as in 1:1 scale. The dispersion models, such as those of the formation of the film and the chemical reaction, play a substantial role and are rather independent of the mesh size. This is not true for the formation of droplets just downstream of the breach. From a previous study [8] it is known that the way how the jet leaving the breach breaks up has an influence on the sequence of events of dispersion and hence changes the dispersed mass fraction. These processes may be influenced by the mesh size, but since there is no experimental evidence of droplet sizes, the present sensitivity analysis can only recommend the use of the parameter sets with the best integral results.

4.4 VARIATION OF THE METAL CONTENT IN THE MELT

If the thermite melt contains no metal components, the steam cannot react with the liquid and there is neither any oxidation energy released nor hydrogen produced. Using the same code input as for the recalculation of the experiment in 1:10 scale, the hydrogen initial contents and production were set zero, and so were the specific energies for oxidation and combustion. **Fig. 23** shows the comparison between measured and calculated pressures. It shows that the dome and cavity pressures rise hardly above 0.3 MPa which is much lower than with hydrogen, see Fig.6, page 10. The only increase in cavity pressures comes after 0.3 s, and it is much higher than in Fig. 6. This results in high velocities which, in turn, entrain the liquid thermite and sweep it out of the cavity.

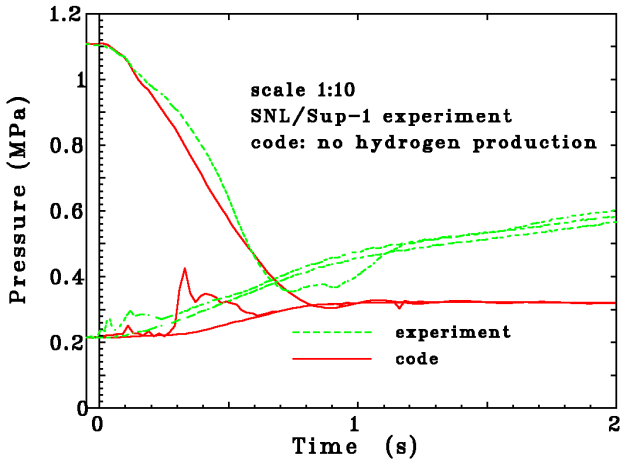

Fig. 23 Pressures of the 1:10 scale case without metal in the thermite

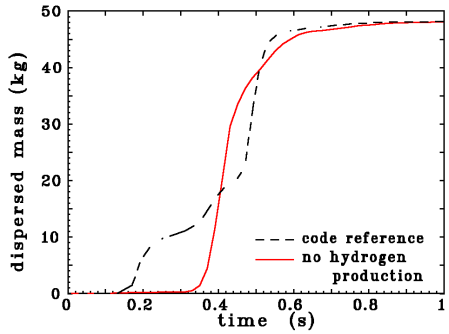

Fig. 24 Dispersed thermite mass of the reference recalculation of the experiment and of the 1:10 scale case without metal

Fig. 24 shows the comparison of calculated dispersed masses, for the reference case and for the transient without hydrogen generation. The reference sweep-out, see also Fig. 7, page 10, starts much earlier and persists until oxidation power fades out, see Fig. 17. For the case without hydrogen production, the dispersion starts only when pressures in the cavity rise due to massive energy transfer from thermite to the gas-vapor mixture. **Fig. 25** shows the total inventory of the cavity. The steam which only can flow out of the pressure vessel after gas blowthrough builds up considerably after 0.3 s, a time when also the bulk of thermite is in the cavity. Consequently, pressures rise when steam is heated up and thermite is ejected into the dome. It is by coincidence that the dispersed thermite mass is just the same as for the reference calculation.

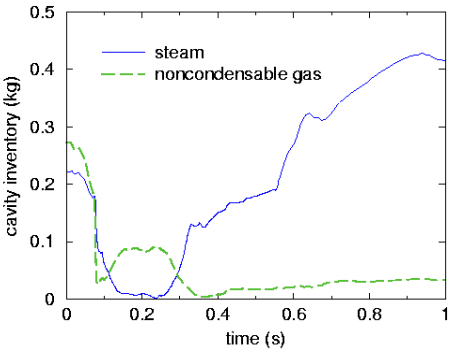

Fig. 25 Cavity inventory of the 1:10 scale case without metal

4.5 UNRESOLVED PROBLEMS

The problems of numerical diffusion have already been addressed, and sensibilities with time steps and cell sizes reported in chapter 4.3. During previous studies with AFDM, the expected behavior of a small cell size limit has been observed. Given a transient problem, the results would converge if a small cell size was reached. Any reduction in cell size would have no effect on the results. However, this is not true for interactions in the vicinity of large gradients [9]. Additionally, the superposed models with averages in clusters of Eulerian cells are independent of the cell size. Since their results have an influence on the next time step cell conditions, delayed feed backs may pose problems for fast transients.

It may be argued that to avoid the problems mentioned above, it would help when the code was only taking into account the clusters of Eulerian cells. This would ultimately lead to systems-level codes like CONTAIN [10]. However, this would also lead to a loss of space

resolution which was found to play a dominant role during the dispersion. In the cavity, for example, high pressure can usually be found close to the breach where the first interactions between melt and steam occur. The consequence of this is multiple. However, the introduction of more integral methods should not be ruled out. If, for example, experimental evidence would favor an entrainment model based upon cavity-average velocities, this part of the present models would need to be changed. In view of the large number of open parameters and uncertain models, fundamental changes to the code are likely not to be made frequently.

In the corner at the periphery of the cavity bottom, the code has to read from the input whether the radial or the axial velocity vector needs to be used. They both are necessary for entrapment and entrainment calculations, where tangential velocities govern the entrainment, perpendicular velocities the entrapment. If the corner cell was reduced to a very small size, it would help reduce the bias of the choice but it would simultaneously reduce time step sizes and increase computational expenditure. On the other hand, the entrapment of a substantial part of the liquid in the corner is a fact, and the choice of the cell size will have a direct influence on the results. Presently, the choice to add a corner cell of normal size to the cells of the vertical annulus has given the best results.

5 EXTRAPOLATING TO PROTOTYPIC CONDITIONS

The scaling up from experimental to prototypic scale is done in two steps. In the present chapter, the linear length is increased by a factor of 10 while the simulant material thermite stays unchanged. In the chapter 5.3, the substitution of the simulant material by the prototypic material, both in prototypic scale, is investigated.

5.1 SCALING OF FUNDAMENTAL VALUES

To scale up from experimental geometry to the prototype, the initial and boundary conditions of the experiments need to be explained with respect to their scaling choice. First, the linear scale of 1:10 is arbitrary and follows the need for technical feasibility. From this scale follows directly that surface areas are scaled 1:100 and volumes are scaled 1:1000. The values are collected in **Table IV**.

Water vapor produces the driving pressure of the prototype. The experiment also uses water vapor, and the temperature frame is similar to that of the prototype, with water temperatures scaled 1:1 and thermite temperatures being close to those of a molten corium pool. The pressure of the experiment is thus scaled 1:1. Linear geometric scale and pressure scale imply that the time is scaled 1:10 and that the velocity is scaled 1:1.

	1:10 thermite	1:1 thermite	1:1 corium
Length, Time	1	10	10
Area	1	100	100
Volume	1	1000	1000
Pressure	1	1	1
Velocity	1	1	1
Mass	1	1000	1900
Droplet size	1	**≈1.7**	**≈1**
$\frac{calculated\ \ melt\ \ fraction\ \ dispersed}{measured\ \ melt\ \ fraction\ \ dispersed}$	1	**≈0.9**	**≈0.8 ***
Hydrogen mass produced in the cavity	1	**≈450**	**≈240**
Mass of the film frozen on the cavity walls	1	**≈200**	**≈50**

Table IV Scaling factors for 1:10 and 1:1 scale

)* the value depends on the scaling hypothesis of [6] and the amount of metal specified in the corium, see Table V

To elucidate the effect of time scaling on the pressure history, a simple blowdown of pure steam out of the pressure vessel is investigated. If the pressure difference across the breach is large enough, the exit velocity, v, is only a function of the upstream conditions. The mass flow out of the vessel is

$$\frac{dm}{dt} = \rho \ \ v \ \ A = \frac{m}{V} \ \ v \ \ A$$

where ρ is the density of steam in the vessel, m is the mass, V the volume, and A the cross section of the breach. Integrating from time zero with the initial mass in the vessel, m_0, yields

$$\frac{m}{m_0} = \exp -(v\frac{At}{V})$$

The exponent consists of the velocity which scales 1:1, and the ratio At/V which also scales 1:1. A similar exponent , α/(ρc)·At/V, results for the temperature transient of a droplet when exchanging heat with the surrounding vapor, where α is the heat transfer coefficient and c the specific heat. Because the heat transfer coefficient depends mainly on the velocity difference between vapor and droplets, values should be rather independent of the scale. Finally, diffusion which plays a role when assessing the exothermic energy of the oxidization of the metal component of the droplets, yields an exponent, Sh C/d ·At/V, where Sh is the Sherwood number for the mass exchange at the droplet surface (see chapter 3.2), C is the diffusion coefficient, and d is the droplet diameter. Again, because velocities scale 1:1, droplet diameters should not change, and Sh should stay constant.

The scale of the molten corium simulant cannot be set to merely the volume scale because experimental and prototypic material properties differ. The scaling approach of the experiments presented in [6] uses a comparison of energies to find the appropriate melt mass. The energy stored in the vessel pressure is scaled like the volume because the energy per volume is equivalent to the pressure and the pressure is scaled 1:1. With this, the equivalence of thermal and chemical energy potential of the dispersed melt demands that the

sum of both be scaled 1:1000. The thermite melt of the experiment is 62 kg with a combined thermal and chemical energy of 178 MJ. The prototype would therefore need 178000 MJ which is equivalent to 119400 kg of corium. Consequently, the mass is scaled 1:1900. The numbers are collected in Table IV. The last column of the table will be used in chapter 5.3.

The combustion rate which is an input parameter depends mainly on the flame surface area, see chapter 4.1. The width of the cavity exit is D=0.1 m. Using the same average exit velocity of v_{fl}=70 m/s as for the 1:10 scale, the Froude number, Fr, is Fr= $v_{fl}^2/(gD)$ and has a value of 500. With this Froude number and according to [7], the flame should be 48 m long. The annular flame surface would thus be around 1900 m^2 which is 60 times the value of the 1:10 scale. The input condition would then be 24 kg/s, but because of uncertainties in exit velocities and increased turbulence due to the linear upscale, a value of 42 kg/s has been chosen.

5.2 SCALING OF RESULTS

After scaling the initial and boundary conditions, the code is used to provide numbers for different physical quantities. **Fig. 26** shows the pressures for the thermite case in 1:1 scale compared to those the calculation in 1:10 scale, see Fig. 6, page 10, and the experiment. The upper abscissa stands for prototypic scale, the lower for experimental scale.

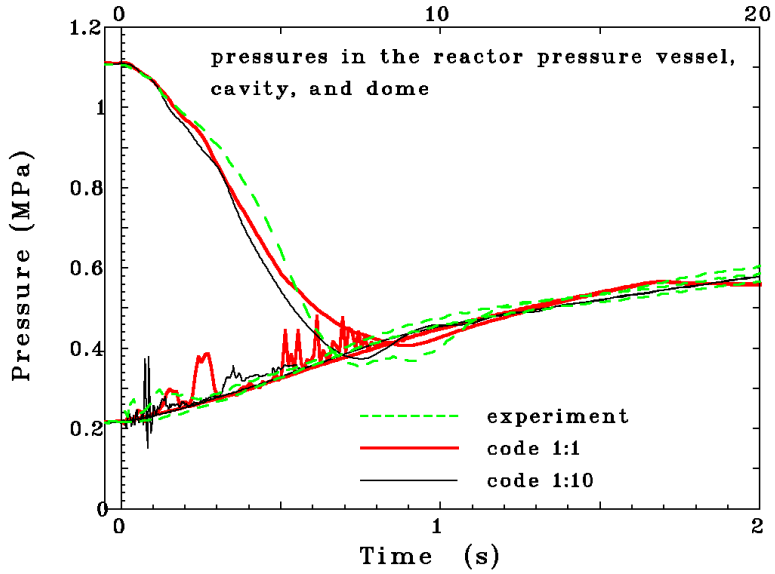

Fig. 26 Pressures of the 1:1 and 1:10 scale thermite cases and the experiment

The figure shows a good agreement between all pressures. The cavity pressure spikes of the 1:1 scale case are more pronounced. For the period between 5 and 8 s of prototypic scale, there are many pressure spikes which lead to a slower decrease of pressures in the reactor pressure vessel. The dome pressures reach their maximum around 17 s when the combustion of the hydrogen generated in the cavity and pre-existing in the dome comes to an end. Hydrogen generation in the dome has not been taken into account in 1:1 scale because of the difficulties of scaling up the parameters used in the recalculation of the experiment. The combustion parameter was scaled 1:10 which will be explained in Fig. 32.

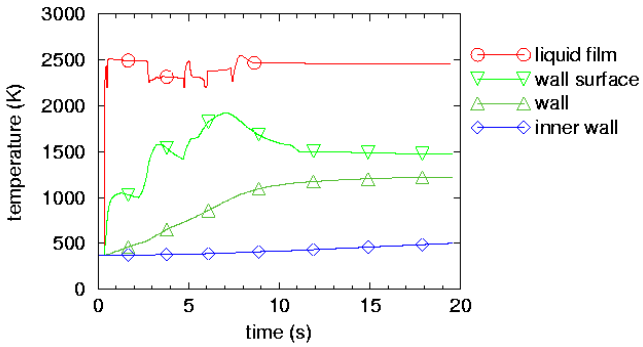

Fig. 27 Film and wall temperatures at the cavity bottom of the 1:1 thermite case

Fig. 19, page 18, had shown the wall temperatures of the experiment. **Fig. 27** shows the temperatures taken at the same location, but now in prototypic geometry. Note that the bottom cavity cell under investigation is now at a radius of 2.5 m instead of 0.25 m. Since the time is also scaled up by a factor of 10, the dispersion transient takes about 12 s. While the liquid film in experimental scale is blown off at 0.6 s it only vanishes between 5 and 8 s in prototypic scale. Afterwards, a film remains at the cavity bottom for radii larger than 1.8 m. Because the liquid film is moving outwards for a long period (up to time=18 s), the film temperature at the given location does not cool down during the given time period. Wall surface temperatures are higher than in the 1:10 scale. **Fig. 28** shows the comparison between experimental and scaled-up thermite crust masses. There are two time scales, for experimental and prototypic scales, respectively. The prototypic ordinate is scaled up by a factor of 100 which is also the scaling factor for the cavity surface area. At time 2 s and 20 s, respectively, the crust masses reach 1.3 kg and 250 kg, respectively. The ratio 250/1.3≈200 is added to Table IV. The total melt mass is scaled up by a factor of 1000 so that there is relatively little mass frozen at the prototypic cavity wall (0.4 %) whereas it was 2% for the experimental scale. Consequently, freezing on cavity walls should have a negligible influence on prototypic dispersion.

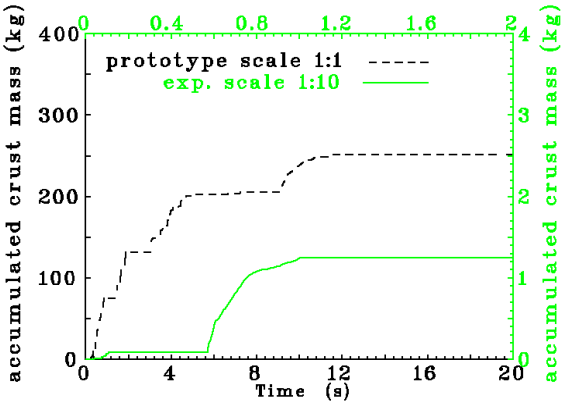

Fig. 28 Accumulated crust mass in the cavity of the 1:1 and 1:10 thermite cases

The dispersion is characterized by the single phase and two phase flow through the breach and the subsequent disintegration of the melt jet into a spray of droplets, by the formation of liquid films at the cavity walls and the entrainment of droplets from the film into the main vapor flow. The droplet size resulting from both processes influences the thermal and chemical interaction with the steam and the way the liquid melt is driven away by the vapor flow. The vapor velocities in the cavity are important parameters of the dominant processes.

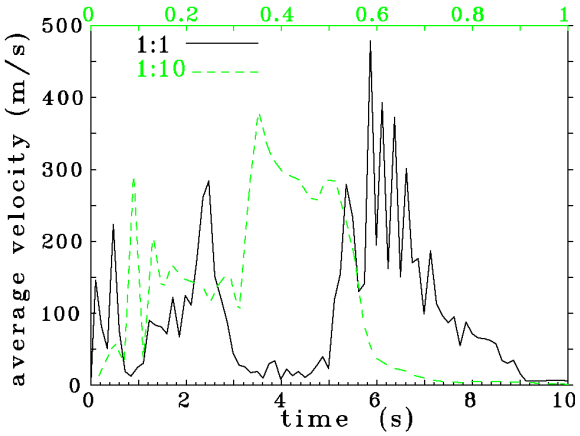

Fig. 29 Average vapor velocities in the cavity of the 1:1 and 1:10 thermite cases

Fig. 29 shows the comparison between cavity velocities in 1:10 and 1:1 scale. The volume-averages are smoothed by a spline approximation. The figure shows about the same velocity levels for both cases, but different time behaviors. Until 3 s in prototypic time, both scales show a roughly similar transient, but afterwards, the experimental scale directly passes to the major velocity peak. In 1:1 scale, the peak only comes after a period of relative calmness.

In the code, the droplet size is space and time dependent so that local effects can be resolved. For the chemical reaction, an average is calculated over all droplets in the cavity, and a single energy equation is solved for the swarm of droplets. **Fig. 30** shows the average droplet size in the cavity for both, 1:1 and 1:10 scale. The upper abscissa stands for 1:10 scale, the lower for prototypic scale. The droplet sizes of both scales are very similar up to the prototypic time of 1.1 s. The associated phenomena of jet breakup close to the breach yield consistent results. Between 0.12 s and 0.5 s, the 1:10 scale droplets are about twice as small as those of the 1:1 scale. During this part of the transient, entrainment processes play a role as well. Beyond 6 s of prototypic scale, the thermite dispersion is still going on in 1:1 scale but has stopped in 1:10 scale. Calculating the time averages of the droplet diameters of both curves yields 2.2 mm for 1:1 scale and 1.3 mm for 1:10 scale. The average of 1:1 scale droplets is therefore a factor of 1.7 larger than for 1:10 scale droplets, the value is added to Table IV.

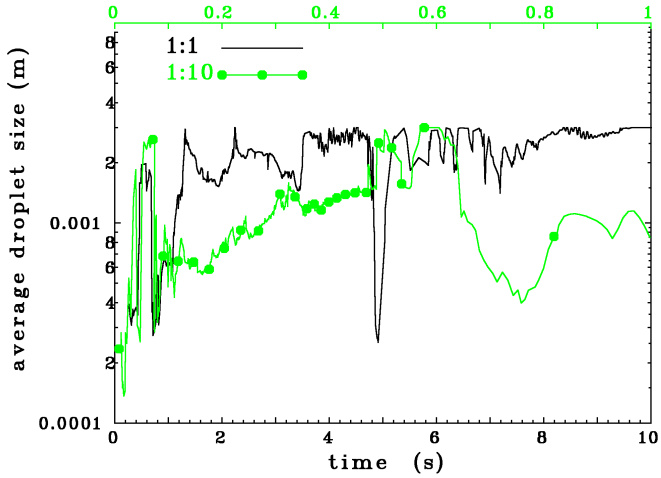

Fig. 30 Average droplet diameter in the cavity of the 1:1 and 1:10 thermite cases

Fig. 31 shows the calculated masses of the liquid thermite film on the cavity walls. The films of both the 1:1 and 1:10 scale rise quickly just after breach opening. They reach a maximum just after gas blowthrough, where the 1:1 scale value is a factor of 1000 higher than that of the 1:10 scale. After a prototypic time of 2 s, there is more entrainment in 1:1 scale, but then film masses rise to first maximum values and beyond. The final entrainment section starts at 0.4 s of 1:10 scale, and at 7 s of 1:1 scale. Not only is the onset of entrainment different for both cases but also the rate of entrainment. In 1:10 scale, the film mass stays almost unchanged after the main entrainment period whereas in 1:1 scale thermite from the main stream is being entrapped to yield rising film masses. This period constitutes the main difference between both cases and yields the inconsistencies of dispersed masses. The film masses given in percent of the initial thermite mass converge against final values of 20% of 1:10 scale and 31% for 1:1 scale. The difference of about 10% can also be found for the dispersed masses (fraction of melt dispersed**:** 1:10 scale=78%, 1:1 scale=69 %).

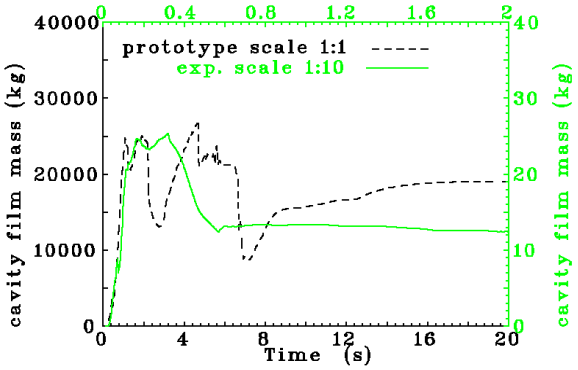

Fig. 31 Film mass in the cavity of the 1:1 and 1:10 thermite cases

Finally, the calculated scaling of the hydrogen generation is presented. **Fig. 32** shows the results for thermite in 1:10 and 1:1 scale. The upper abscissa stands for experimental scale, the lower for prototypic scale. The right ordinate stands for 1:10 scale, the left for 1:1 scale. In the experiment, the amount of hydrogen has been evaluated for time=20 s and later. A value of 0.89 kg was found which is shown as two dots close to the right ordinate. Hydrogen mass change due to combustion is not taken into account in this graph. The 1:10 scale curve has already been explained with Fig. 16, page 17. It has an intermediate plateau at 0.44 kg which is the amount of hydrogen generated inside of the cavity. It is 34% of what could be produced if all metal was oxidized. The value of 0.44 kg has to be compared to the 270 kg of hydrogen in 1:1 scale. For the 1:1 scale calculations, only hydrogen generated in the cavity has been taken into account. The 1:1 scale hydrogen mass is a factor of 450 higher than the 1:10 scale mass, the value is added to Table IV. This is smaller by a factor of 0.45 than the mass scaling. The rate with which hydrogen is generated in the cavity is about a factor of 100 higher. However, hydrogen production in the cavity comes in two steps, during the first second, and between 3 and 5 seconds. In the experimental recalculation, the production is almost constant up to 0.5 s. The timing of both calculations is consistent with the expected ratio of time scales of 1:10. The transient is characterized by a steam shortage in the cavity so that not all metal fraction of the melt is oxidized. If all metal of the prototypic scale would react, a total of 1280 kg of hydrogen would be produced, but only 21% are actually calculated to be produced.

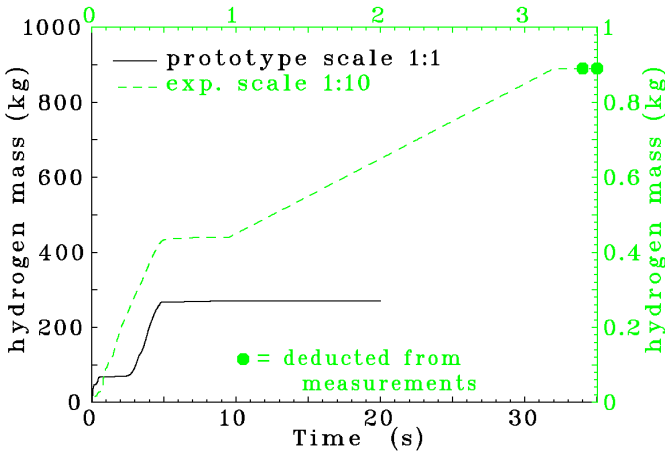

Fig. 32 Hydrogen generated of the 1:1 and 1:10 thermite cases

5.3 REPLACING THERMITE BY CORIUM

The rational for scaling of the corium mass has been presented in chapter 5.1. For corium, not only the reaction energy changes but also the amount of metal in the melt, and hence the amount of hydrogen generated per mol of corium. As shown in Table 8 of [6], there are 894 kmol of thermite in 1:1 scale with 0.7111 mol H_2 produced per mol melt.

constituent	mass fraction		mol fraction	
	corium	thermite	corium	thermite
UO_2	0.8477	0	0.7056	0
ZrO_2	0.1272	0	0.2323	0
Zr	0.0251	0	0.0620	0
Fe	0	0.5315	0	0.6554
Al_2O_3	0	0.4540	0	0.3074
Al	0	0.0145	0	0.0371

Table V Melt composition for corium and thermite

For corium, there are 531 kmol and 0.1241 mol H_2 produced per mol melt. This indicates that there is a reduction by a factor of almost 10 of hydrogen generation when using corium of the Sandia specification which was taken from the Calvert Cliffs scenario V upper bound limits presented in [11]. A total of 635 kmol of hydrogen equivalent to 1280 kg can ultimately be produced with thermite, but only 66 kmol of hydrogen equivalent to 133 kg with corium. **Table V** lists the specifications of [6] with mass and mole fractions.

property	**dimension**	**thermite**	**corium**
oxidization enthalpy	J/kmol	$1.6 \cdot 10^7$	$3.8 \cdot 10^7$
hydrogen generation potential	mol H_2/mol melt	0.7111	0.1241
melt molecular weight	kmol/kg	69.1	224.7
density	kg/m^3	3878	8045
liquid specific heat	J/(kg K)	1198	526
liquidus temperature	K	2200	2450
heat of fusion	J/kg	$1.056 \cdot 10^6$	$2.77 \cdot 10^6$
thermal conductivity	W/(m K)	19.7	5
viscosity	Pa s	$1.0 \cdot 10^{-3}$	$3.14 \cdot 10^{-3}$
surface tension	N/m	1	1

Table VI Properties and equation of state values of thermite and corium

Additional to these data, the material equation of state and properties change. **Table VI** shows a selection of values used in the code. The biggest difference can be noted for the density and the hydrogen generation potential. In view of the prevailing uncertainties, the surface tension was set to 1 N/m for both materials.

Fig. 33 shows a comparison between pressures of the corium case and the thermite case in 1:1 scale together with experimental values. The transients look similar until 2.6 s. Afterwards, the corium cavity pressures rise rapidly. The main reason is a combination of higher liquid corium temperatures with less oxidation energy produced in the cavity. Looking at the ensemble of calculations with the whole spectrum of oxidation energies and temperatures, one could argue that oxidation after gas blowthrough which is likely to occur close to the breach increases local pressures and thus reduces mass flow through the breach which, in turn, may reduce average cavity velocities and thus heat transfer between droplets and steam. Higher melt temperatures, on the contrary, increase steam pressures downstream of the oxidation area. The integral result of these interacting phenomena is that less melt is dispersed beyond the cavity exit.

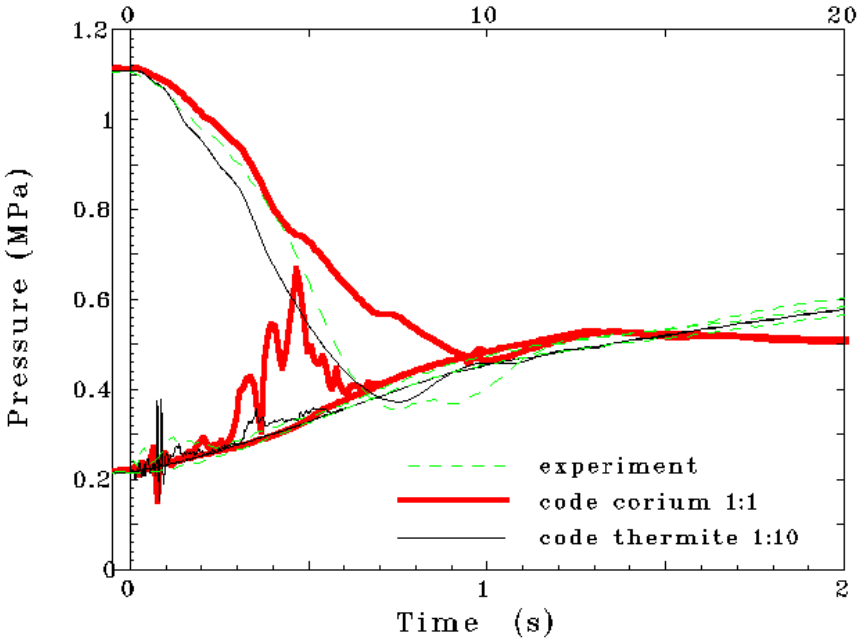

Fig. 33 Comparison of pressures of the 1:1 corium and 1:10 thermite cases

The cavity pressures of the corium case of Fig. 33 show a faster increase than thermite pressures after 5 s because of the higher melt temperatures. The high cavity pressures prevent vessel pressures to fall as rapidly as for the thermite cases. Pressures of all regions converge only after 9 s which is 3 s later than for thermite. After 13 s, the pressures level out because all hydrogen has already been burnt. Therefore, maximum pressures in the cavity and dome stay below those of thermite cases.

Fig. 34 shows a comparison of relative dispersion fractions in 1:1 scale thermite and corium calculations. Corium dispersal is mainly done between 2 s and 5 s, but thermite dispersal still goes on afterwards. Corium dispersion resembles the case without hydrogen production of Fig. 24, page 23, with a later but more violent dispersion. 78100 kg were calculated to be dispersed beyond the cavity exit. The dispersed mass fraction of corium yields 65% which is

about 80% of what was measured in the experiment. The relative value of 0.8 is listed in Table IV.

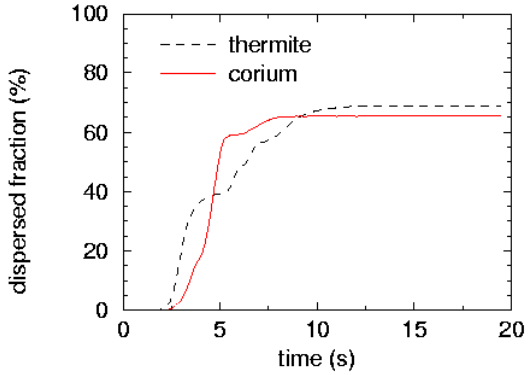

Fig. 34 Dispersed melt fractions of the 1:1 corium and 1:1 thermite cases

The droplet size depends among others on the surface tension which stays practically unchanged when replacing thermite by corium. Surface tensions have been set invariable with temperature. **Fig. 35** shows a comparison between thermite and corium droplet sizes, both in 1:1 scale. Initially, corium droplets are slightly larger, but after 1 s, they are about a factor of 2 smaller. It is the higher average cavity vapor velocity of the corium case which decreases droplet sizes. The droplet size calculated for the 1:1 corium case is remarkably close to the one evaluated for the experiment, so a scaling factor of ≈1 is added to Table IV.

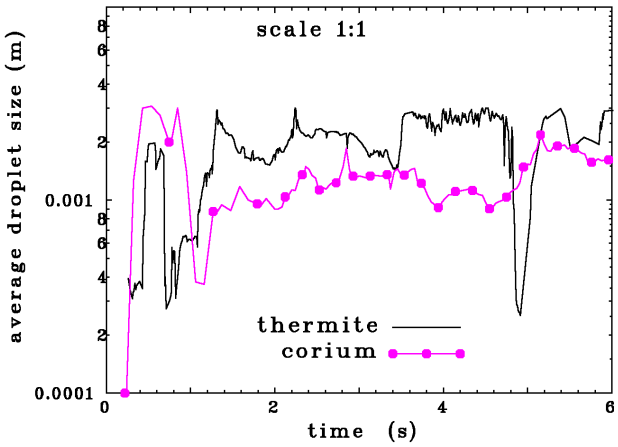

Fig. 35 Comparison of droplet diameters of the 1:1 corium and 1:1 thermite cases

Corium oxidation is also steam limited although the melt contains less metal. **Fig. 36** shows the cavity inventories of steam and gases during the first 8 s. The initial steam inventory is reduced before gas blowthrough which takes place around 0.6 s. Until 3.6 s, all steam flowing in is consumed by oxidation. Hydrogen inventory peaks just after gas blowthrough and when cavity pressures rise rapidly. After 3.6 s, the reaction is no longer steam limited, but most of the metal components are already oxidized.

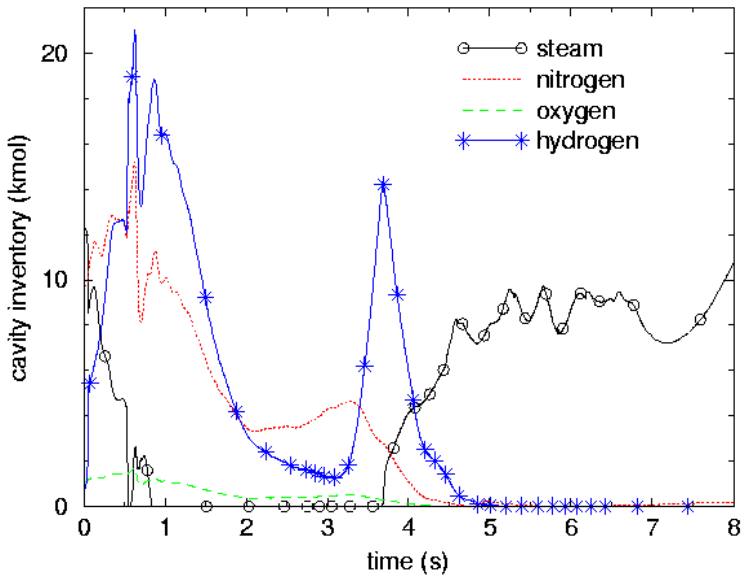

Fig. 36 Cavity inventories of the 1:1 corium case

Hydrogen production falls down close to zero around 5 s. **Fig. 37** shows the comparison between thermite and corium, both in 1:1 scale. The dynamics of both productions is very similar, but as there is less metal in corium, there is less hydrogen production. In the corium

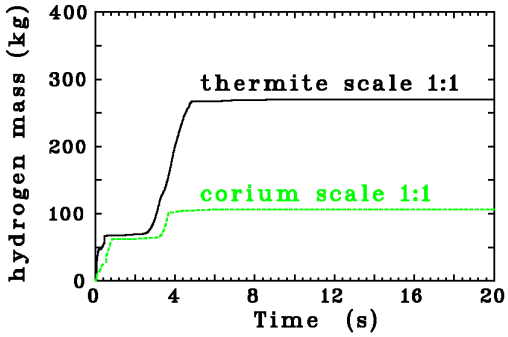

Fig. 37 Hydrogen generated of the 1:1 corium and 1:1 thermite cases

case, there are 53 kmol hydrogen equivalent to 106 kg generated which represents 80% of the potential when oxidizing all metal components. This value has to be compared to the 0.44 kg of in-cavity hydrogen production of the experiment. The corium case produces thus a factor of 240 more hydrogen than the experiment, and this number is added to Table IV. As for the 1:1 thermite calculations, the hydrogen combustion rate has been fixed at 42 kg/s. Hydrogen combustion fades out at 13 s.

Fig. 38 shows the mass flows out of the cavity into the reactor dome. There is relatively less hydrogen compared to the thermite cases. The present model does not take into account the oxidation through oxygen. Therefore, oxygen is being blown out together with the nitrogen. Oxidation is calculated through steam alone, and very little steam is blown out during the first 3 seconds.

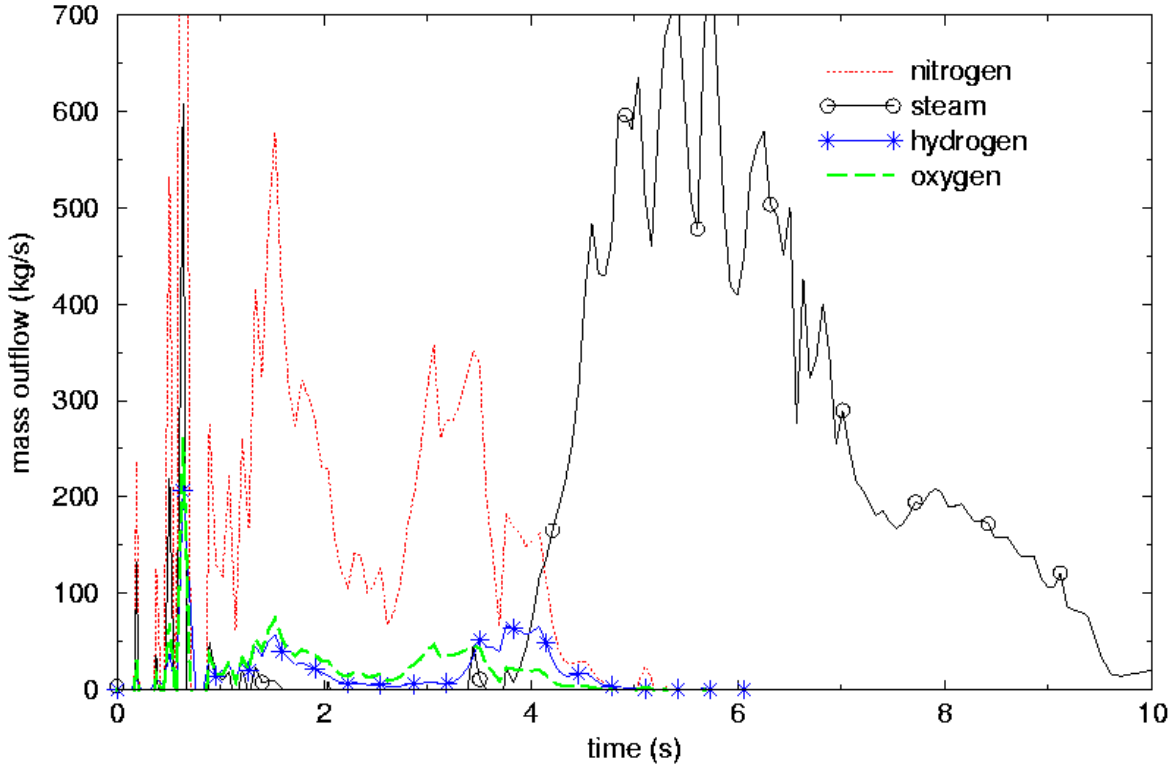

Fig. 38 Mass flow out of the cavity for the 1:1 corium case

Because there is less hydrogen produced, the energy balance looks different to that of thermite. **Fig. 39** shows power and energy of both the oxidation and combustion for corium in 1:1 scale. Because initial conditions are just the scale-up of the experiment, there are 410 kg of hydrogen in the reactor dome prior to the transient. At the given combustion rate of 42 kg/s, it takes 9.8 s to burn only this part of the hydrogen. This is why, especially for corium at

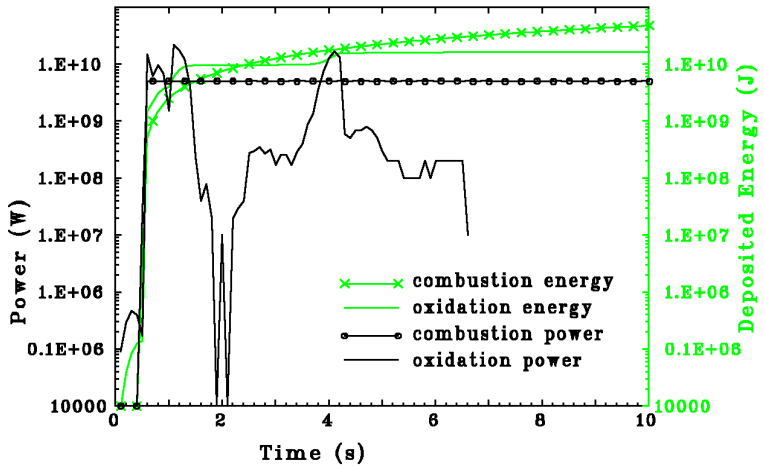

Fig. 39 Power and energy of metal oxidation and hydrogen combustion of the corium case

low metal content, the pre-existing hydrogen plays a substantial role. During the first 1.5 s, both power levels are similar. The subsequent second is characterized by a substantial reduction of the reaction level. Between 2.5 and 6.5 s, the power level is smaller for oxidation than for combustion. Different to thermite, the deposited energies grow to the same orders of magnitude. The total oxidation energy sums up to 16300 MJ, combustion energy up to 63700 MJ.

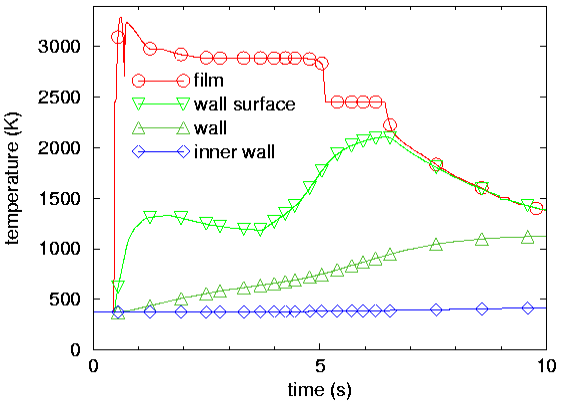

Fig. 40 Film and wall temperatures at the cavity bottom of the 1:1 corium case

Fig. 40 shows the film and wall temperatures at the bottom of the cavity at a radius of 2.5 m. The liquid film is built up after 0.4 s. The early thin film is very hot because of energy release from the oxidation. At 2 s, the film temperature falls back to slightly above the initial corium temperature which is 2800 K. The film thickness reaches its maximum at 3 s and vanishes at 5 s. A very thin crust remains. During the period of film presence the wall surface reaches about 1300 K. The total crust mass in the cavity does not exceed 60 kg which is only 25% of the thermite case in 1:1 scale. This is about a factor of 50 larger than for the experiment, the value is added to Table IV, and only 0.05% of the initial corium mass. Most of the crust can be found in the lower lateral corner of the cavity.

5.4 VARIATION OF THE INITIAL TEMPERATURE

The initial corium temperature is decreased from 2800 K to the thermite value of 2500K. This produces similar steam heat up conditions as for the experiment. **Fig. 41** shows the pressures for this case. The vessel pressure is lower than for the case with 2800 K, and the

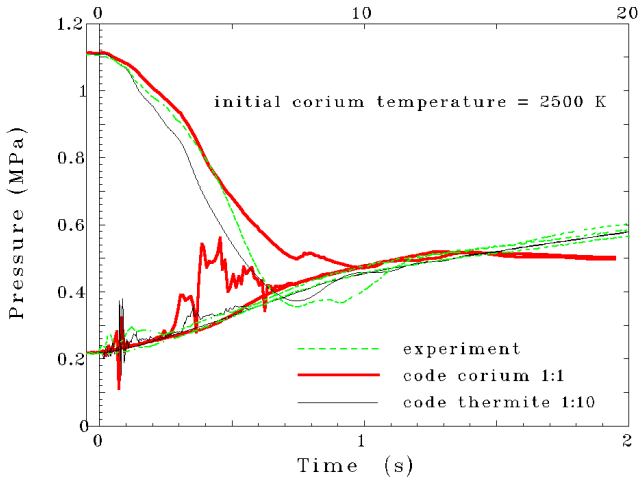

Fig. 41 Pressures of the 1:1 corium case with 2500 K compared to the experiment

cavity pressure rise is slightly less pronounced. Only 44800 kg of corium are dispersed out of the cavity which is 38% of the initial mass and 58% of what has been dispersed in the 2800 K case. The reaction in the cavity are less violent, so there is more time for oxidation so that 110 kg of hydrogen are being produced which is slightly more.

5.5 VARIATION OF THE STEAM CONTENT

There are initially 74 mol of steam in the pressure vessel in the experiment which translates to 74 kmol for prototypic scale. For the reference calculations, both in 1:10 and 1:1 scale, 139 mol and 110 kmol water, respectively, have been added to the accumulator the reason of which has been explained in chapter 4.1. An additional corium case was run with no added water. **Fig. 42** shows the pressures of this case together with measured and calculated pressures of the experiment. The figure shows that vessel pressures fall rapidly after 3 s, that the cavity pressure rise does not stay as long as for the reference corium case, and that dome pressures stay permanently below all reference dome pressures. Consequently, there are only 37000 kg or 31% corium dispersed out of the cavity. The total amount of hydrogen generated in the cavity adds up to 102 kg.

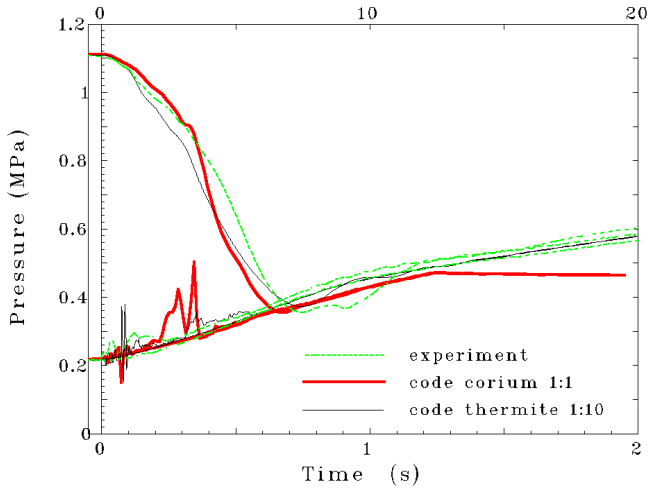

Fig. 42 Pressures of the 1:1 corium case with less steam compared to the experiment

5.6 VARIATION OF THE HYDROGEN CONTENT

The hydrogen content which was 410 kg in the reactor dome can contribute considerably to the pressure rise because corium of the present specification does not allow much oxidation

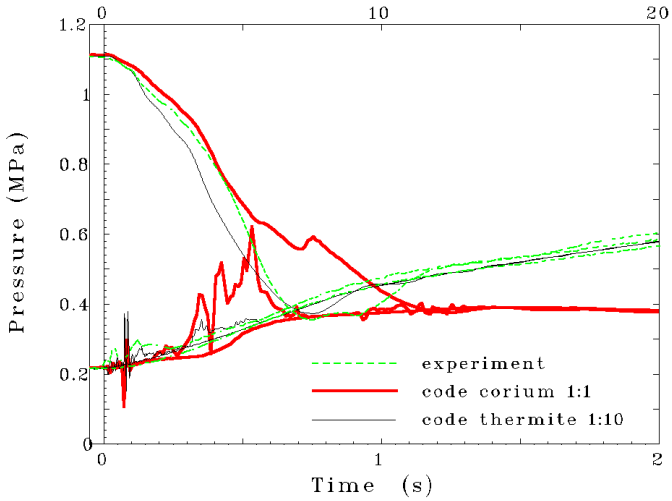

Fig. 43 Pressures of the 1:1 corium case without pre-existing H_2 compared to the experiment

and the code cannot distinguish between pre-existing and produced hydrogen. Therefore, an additional calculation with no pre-existing hydrogen was added.

Fig. 43 shows the pressures for this case. The initial corium temperature is 2800 K, and also all other parameters are the same as for the reference corium calculation. For the first 2 s, the pressures are similar to the reference corium case of Fig. 33, page 31. Between 2 s and 5 s, the pressures in the dome are lower. After 6.5 s, all hydrogen has been burnt and pressures in the dome have reached a maximum value of 4 bar which is 1 bar below the reference case. The vessel pressures are very similar to those of the reference case. However, they join dome pressures only after 11 s, compared to 9 s for the reference case, because they need to decrease 1 bar more. **Fig. 44** shows the energy and power of oxidation and combustion. This figure has to be compared to Fig. 39, page 34. It shows that, contrary to the reference case, the combustion power does not always stay at the maximum value of 5000 MW which corresponds to the input combustion rate of 42 kg/s. This means that at this rate all hydrogen available in the dome is burnt, i.e. that all hydrogen being produced in the cavity and flowing into the dome is instantly being consumed. Oxidation and combustion stop just after 7 s. The dispersed mass is 81600 kg which represents 68% of the initial corium mass. This is a little bit higher than the reference case, but the difference is lower than the uncertainties. It depends on the energetics inside the cavity and is therefore subjected to the local conditions, see chapter 4.5. Generally speaking, the reduction in hydrogen inventory does not clearly influence dispersion. Secondary effects seem to dominate changes in dispersion characteristics. However, big differences are being observed for the pressure history.

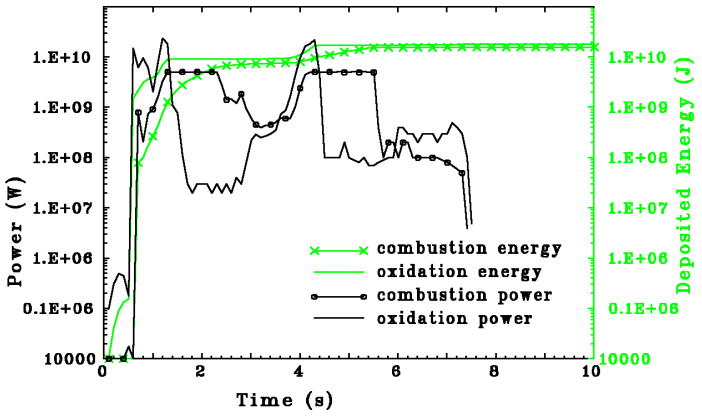

Fig. 44 Power and energy of oxidation and hydrogen combustion of the corium case without pre-existing H_2

5.7 VARIATION OF THE METAL CONTENT

The definition of the corium composition used in the calculations is based upon the Sandia specification which was taken from the Calvert Cliffs scenario V upper bound limits presented in [11]. The only metal taken into account is zirconium with a mol fraction of 0.062, see Table V. If more metal is found in the corium the chemical reaction would increase. Therefore, a couple of runs were added to the reference calculation to identify the influence on the fraction of melt dispersed out of the cavity. The additional metal is supposed to be iron which may represent molten structures inside the pressure vessel. The total melt mass of 119400 kg is

not changed, except for the two cases with 130000 kg. The surface tension and all other thermophysical quantities are being kept like given in Table VI, but the mixture density has been adjusted. The relative mol fractions of the original corium plus zirconium, relative to the corium part alone, have been kept constant.

Given the mol fraction of the added iron which is the parameter of the new runs, the number of mol hydrogen produced per mol melt has to be evaluated. The specific reaction yields a stoichiometric potential of 2 mol hydrogen produced per mol zirconium, and 1 mol hydrogen per mol iron if the iron is oxidized to FeO, a reaction which is dominant given the short time in which it may take place. The hydrogen generation rate of the corium mixture is now the sum of the product of the mol fraction and the stoichiometric hydrogen potential. **Tables VII** and **VIII** show the parameters used in this analysis.

case	initial melt mixture quantity (kg↔kmol)	mol fractions				reaction energy of mixture (MJ/kg)	thermal energy of mixture (MJ/kg)	fraction of melt dispersed
		Zr	Fe	UO_2	ZrO_2			
no metal	119400 ↔ 512	0	0	.7523	.2477	0	1.33	0.52
standard corium	119400 ↔ 531	.062	0	.7056	.2323	0.16	1.33	0.65
iron added	119400 ↔ 662	.0458	.2626	.5203	.1713	0.15	1.38	0.59
iron added	130000 ↔ 721	.0457	.2627	.5202	.1714	0.15	1.38	0.44
large iron mass	130000 ↔ 1216	.0187	.7016	.2098	.0699	0.12	1.57	0.33

Table VII Standard corium in 1:1 geometry compared with cases of less or more metal

The reaction is exothermic and the energy released for the corium mixture including zirconium of a mol fraction of 0.062 is 37.1 MJ/kmol, see also [6], where the specific reaction energy is 598 MJ/kmol for zirconium. With iron, only a small specific reaction energy of 1.97 MJ/kmol is added to the mixture. Therefore, as shown in Table VII, the reaction energy does not change much when adding iron. For the last case, the mol fraction of zirconium is reduced considerably which has an effect on the reaction energy. The energies listed exclude the part produced by hydrogen combustion in the reactor dome because this does not relate directly to the dispersion. The thermal energy is calculated with the assumption that all energy stored in the melt when heating it up from 280 K to 2800 K is available, and the mass affected is the total initial melt mass.

case	initial melt mass (kg)	mixture volume (m^3)	mixture density (kg/m^3)	mixture specific heat (J/(kg K)	mol H_2 produced per mol mixture	maximum H_2 amount possible (kg)	H_2 produced after 20 s (kg)	ratio H_2 produced to max. amount possible
no metal	119400	14.84	8045	526	0	0	0	0
standard corium	119400	14.84	8045	526	0.124	133	106	0.80
iron added	119400	15.24	7836	547	0.354	472	201	0.43
iron added	130000	16.59	7836	547	0.354	515	177	0.34
large iron mass	130000	18.11	7180	622	0.739	1812	285	0.16

Table VIII Mixture properties and H_2 production in 1:1 geometry

Table VIII lists the density and liquid specific heat of the melt mixture together with the hydrogen ratio and the total amount of hydrogen calculated by the code (second last column).

The hydrogen potential depends on the metal content of the melt. The potential of the mixture is an input parameter to the code. The values for the five cases are listed in Table VIII, column “mol H_2 produced per mol mixture”. Together with the initial amount of the mixture, this value leads to the “maximum H_2 amount” that can possibly be produced by oxidation. It is also listed in Table VIII, adjacent to the value which is calculated by the code. Except for the standard corium case, the actually produced hydrogen mass is only a small fraction of what could be produced if the coherence would be higher, i.e. if steam would be in contact with liquid melt droplets inside the cavity for a longer period of time. When iron is added and the total melt mass is increased, the ratio of hydrogen actually produced to the maximum amount possible (last column) falls considerably.

The last column of Table VII shows that there is less dispersion, compared to the standard corium case, if there is no oxidation in the cavity. The cases with standard corium and iron added, both with 119400 kg of melt, yield nearly the same dispersions. When increasing the melt mass, the calculated dispersed fraction decreases. The case with the large iron mass yields the smallest fraction of melt being dispersed. To shed some light on the differences, several figures will present the cavity inventories of melt droplets, film, steam, and hydrogen. **Fig. 45** and **Fig. 46** are the figures with 119400 kg of melt. They both have similar histories, with the iron case keeping the droplet inventory for a longer time. The lack of steam lasts 3.6 s for the standard corium, and 4.3 s for the iron case. Because of the higher hydrogen ratio (see Table VIII), the iron case exhibits a larger hydrogen inventory around 4 s. The differences in dispersion seem to come from the tail end of the droplet curves which show that the standard case inventory decreases more rapidly. When the droplet inventory decreases, the droplets are either blown out of the cavity or entrapped into the liquid film. The iron case shows a higher film inventory level and an increase in film inventory around 8 s.

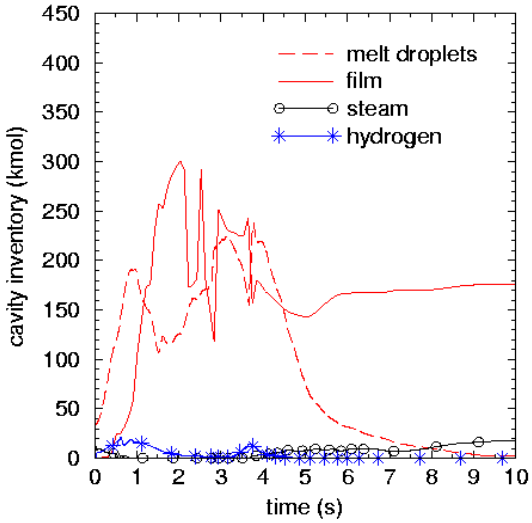

Fig. 45 Cavity inventory of the 1:1 standard corium case with 119400 kg

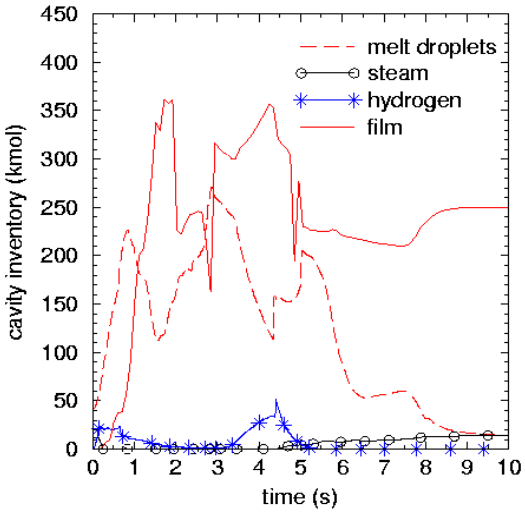

Fig. 46 Cavity inventory of the 1:1 added iron case with 119400 kg

Fig. 47 represents the iron case with 130000 kg of melt. The transient looks similar to the iron case with 119400 kg. The present case has more hydrogen between 0.6 s and 2 s, and a higher film inventory level. While the droplet inventory level stays unchanged, there are more droplets in the 130000 kg case between 4.5 s and 6.3 s. The film inventory level of the 130000 kg case is substantially higher.

Fig. 48 shows the calculations for the case with 130000 kg of melt and a large iron mass. While the first 3s look similar to the iron case with 130000 kg, the tail end shows a higher hydrogen inventory because of the larger hydrogen ratio, and much more mobile droplet inventory. The steam shortage now lasts for 5.7 s, compared to 4.5 s for the case with less iron. Late time entrainment and entrapment processes are responsible for sudden changes in the inventories of droplets and film.

The comparison of the four figures has shown that the hydrogen inventory increases with increasing iron content, and that the time interval that there is a severe lack of steam grows longer. The period of steam shortage is characterized by the consumption by chemical reaction of all the steam in the vicinity of the breach where it enters the cavity. While steam and hydrogen inventories show trends, the droplet and film inventories do not give a clear

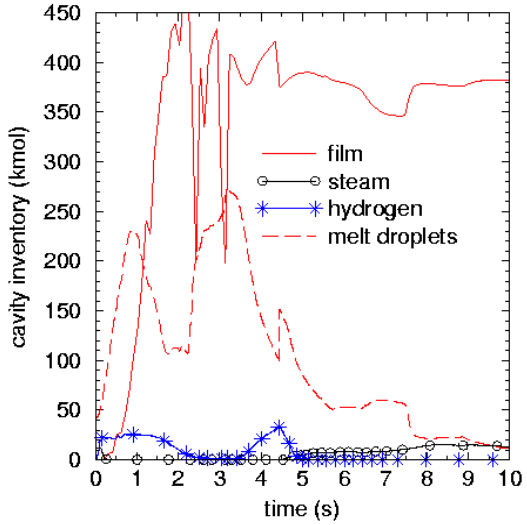

Fig. 47 Cavity inventory of the 1:1 added iron case with 130000 kg

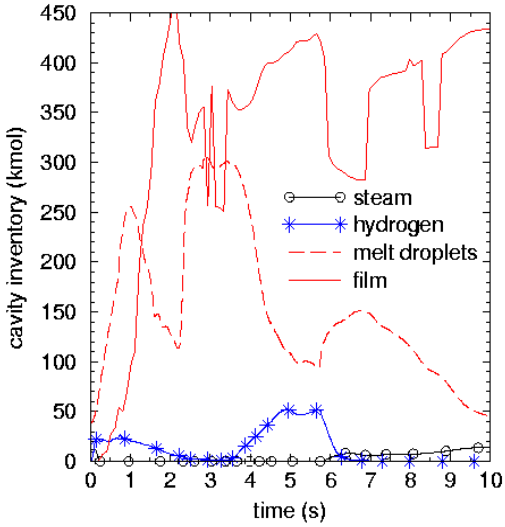

Fig. 48 Cavity inventory of the 1:1 large iron case with 130000 kg

picture. Because entrapment and entrainment are calculated cell by cell, local conditions, even if they are subjected to discretization deficiencies, can be responsible for the

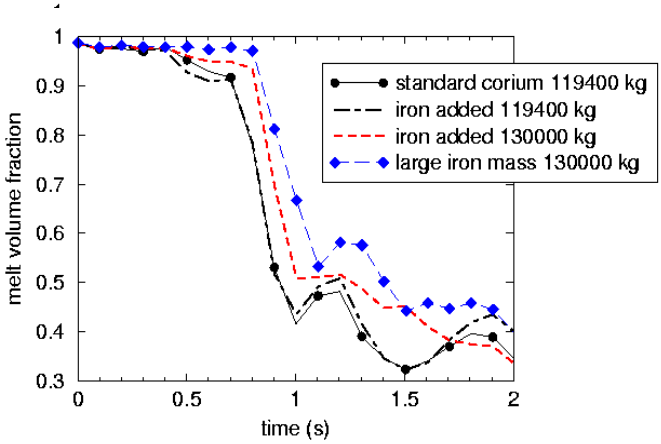

Fig. 49 Melt fractions in the breach of the 1:1 scale variation of the metal content

differences. If these models were defined for cavity averages only, the influence of the geometry would have to be taken into account by a parameter. At this stage of the analysis, a step towards a more integral approach should not be ruled out.

With **Fig. 49**, the comparison of the blowthrough times of the four cases is discussed. The figure shows the melt volume fractions in the lower breach cell. The melt volume fractions start close to 100%. From 0.7 s on, the volume fraction drops rapidly. This indicates the vapor-gas blowthrough. The figure shows that the cases with standard corium and iron added, both with 119400 kg melt, see the same timing, and that the case with added iron and 130000 kg has a blowthrough delayed by 60 ms. The blowthrough of the last case with a large iron mass comes 20 ms thereafter but the downward gradient is smaller. The blowthrough times relate well to the initial mixture volumes listed in Table VIII.

Fig. 50 shows the average temperatures of the droplets in the cavity. The exothermic heat flows to the liquid phase of the droplets. The droplets exchange heat with the vapor which

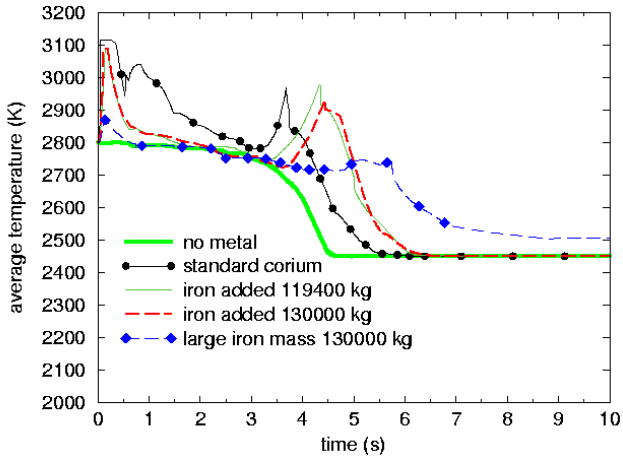

Fig. 50 Average droplet temperatures of the 1:1 scale variation of the metal content

raises cavity pressures. During entrapment, the droplets add their internal energy to the film at the wall. Except for the cases without metal and with a large iron mass, the total energy

released by chemical reaction has a value of about 20000 MJ. Therefore, the liquid and gas cavity temperatures of those cases do not differ much. They are up to 300 K higher than without chemical reaction.

Fig. 51 shows the hydrogen mass flow out of the cavity into the reactor dome for the four cases. While all cases have the same flow level up to 4 s, the standard corium hydrogen flow drops to zero thereafter, but all other cases go through a maximum. For the two cases with added iron, the peak value of the 119400 kg case is higher than for the 130000 kg case which is unexpected. The blowdown of the large iron mass case takes nearly two seconds longer than the other cases.

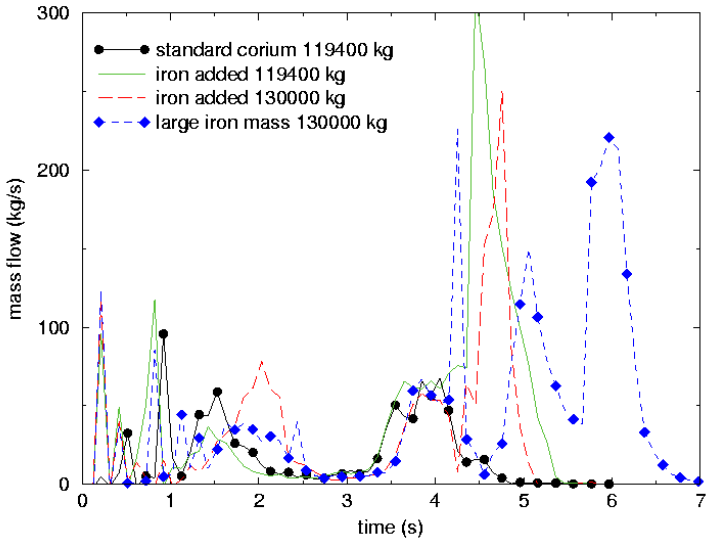

Fig. 51 Hydrogen mass flow of the 1:1 scale variation of the metal content

6 CONCLUSION

The more energetic experiment of the Sandia SNL-Sup tests has been recalculated with a CDF code of the SIMMER family. The analysis confirms the findings by the experimentalists that the oxidation in the cavity is steam limited, that in order to obtain measured final hydrogen inventories, oxidation must be considered in the dome of the reactor containment, and that hydrogen is burnt at a relatively constant rate in the dome. It also confirms that the melt droplets as well as the hydrogen flame may come close to the dome ceiling. The conditions in the pressure vessel during the main period of melt dispersion leaves open questions because the code needs additional water in the vessel to achieve the late vessel pressure decrease. A combination of entrapment and entrainment models previously used to recalculate DISCO-C experiments with water instead of thermite as corium simulant proves to also be valid for the dispersion of thermite out of the cavity into the dome. Different to the water test calculations, the formation of droplets in the vicinity of the breach needs to be changed to yield smaller droplets for thermite. With the agreement obtained for the measured quantities, the code provides an abundance of transient data of film and crust inventories, steam, nitrogen, oxygen, and hydrogen contents and mass flows. It also provides the energies of oxidation and combustion, the time dependent hydrogen generation, and the temperature distributions including walls adjacent to the melt films. A sensitivity analysis

shows problem areas during discretization of space and time. Additional unresolved issues are addressed.

An attempt is undertaken to extrapolate to reactor conditions. The first step to scale up to prototypic scale while maintaining thermite as melt constituent yields expected results according to the basic scaling laws. Differences are found in the time behavior of cavity inventories and chemical reactions. This yields different velocities to drive entrainment processes and droplets sizes so that the dispersion is slightly reduced. Hydrogen generation is relatively lower and solid crusts are found to play no role, neither for corium, for the amount of melt dispersed out of the cavity. When replacing thermite by corium in prototypic scale, new sensitivities arise beyond those already mentioned. These depend on the specification of the melt, and are thus subjected to the history of the accident. The relevant results scale as predicted, the pressures look similar to the experiment except for the cavity pressures which are higher mainly because of the higher initial melt temperature. The relative amount of hydrogen generated depends strongly on the melt mass and the metal content in the melt, and the fraction of melt discharged into the dome is lower but reasonably close to what has been measured. However, results show a considerable scatter and sensitivities with geometric resolution and dynamics of energy transfer between participating components. It is therefore necessary to demand for a more important number of thermite tests.

The results of the dispersion and hydrogen generation, including the recalculation of the experiment, are collected in **Table IX**. The table shows that the dispersion is successively reduced when going from the experiment to more prototypic conditions, and even beyond when more iron due to molten in-vessel structures is added to the melt. Because the code is limited to calculate oxidation only in the cavity, hydrogen generation data need to be compared to the reference recalculation. The comparison reveals a reduction in the generation when scaling up the geometry. Additional iron will raise the hydrogen output, yet with a low efficiency. The study included many more computer runs than presented here. The scatter of dispersed melt fractions obtained by changing input parameters not directly associated to dispersion models must be taken into account. It should be around ± 30 %.

case	scale	initial melt mass (kg)	dispersed melt mass (kg)	dispersed melt fraction (%)	H_2 produced at half time (kg)	ratio H_2 produced to max. amount possible
experiment	**1:10**	**62**	**48**	**78**	**(0.89)**	**(0.70)**
reference recalculation	1:10	62	48	78	**0.44**	**0.34**
reference recalc., no metal	1:10	62	48	78	0	0
standard thermite	1:1	62000	42800	69	270	0.21
standard corium	1:1	119400	77600	65	106	0.80
corium at lower temperature	1:1	119400	44800	38	110	0.83
corium, no added water	1:1	119400	37000	31	102	0.77
corium, no pre-existing H_2	1:1	119400	81600	68	116	0.87
corium, no metal	1:1	119400	62100	52	0	0
corium, iron added	1:1	119400	70400	59	201	0.43
corium, iron added	1:1	130000	57200	44	177	0.34
corium, large iron mass	1:1	130000	42900	33	285	0.16

Table IX Integral results of the present study

(...) = post test assessment of total amount at full time

From the DISCO-C experiments, a qualitative picture of the formation of liquid films on the cavity walls has evolved. For the thermite tests, there is no such picture. The development of entrapment and entrainment models beyond the present parametric approach would require detailed transient data. The same is true for the development of droplet sizes. Because both processes have a dominant influence on dispersion, the degree of freedom of choice of the many parameters renders difficult any straight forward extrapolation. When replacing thermite by corium, it is unknown whether the importance of any of the physical processes with respect to the others changes. Because the present analysis has not succeeded in showing that the history of events is, given the proper space and time scaling, similar with all materials and scales, the extrapolation to prototypic conditions can only be based on a large number of experiments.

7 REFERENCES

[1] Meyer L., Jacobs G., Wilhelm D., Gargallo M., Blanchat T.K., Experiments on Corium Dispersion after Lower Head Failure at Moderate Pressure, Proc. of the Seminar on Containment of Nuclear Reactors held in Conjunction with the 15th International Conf. on Structural Mechanics in Reactor Technology, Seoul, Korea, Aug. 23-24, 1999, pp. 245-265

[2] Bohl W.R., Wilhelm D., The Advanced Fluid Dynamics Model Program: Scope and Accomplishment, Nuclear Technology, Vol. 99, 1992, pp. 309-317

[3] Hewitt G.F., Liquid mass transfer in annular two phase flow, in F. Durst et.al. (Ed.), Two-phase momentum, heat, and mass transfer in chemical, process, and engineering systems, Vol.1, Washington, 1979, p. 273

[4] Meyer L., Experiments to Investigate the Low Pressure Corium Dispersion in EPR Geometry, Proc. of the OECD Workshop on Ex-Vessel Debris Coolability, Karlsruhe, Nov. 15-18, 1999, wissenschaftliche Berichte, FZKA-6475 (May 2000), pp. 36-44

[5] Williams D.C., Griffith R.O., Assessment of Cavity Dispersal Correlations for Possible Implementation in the CONTAIN Code, Sandia National Laboratory report SAND94-0015, February 1996

[6] Blanchat T.K., Pilch M.M., Lee R.Y., Meyer L., Petit M., Direct Containment Heating Experiments at Low Reactor Coolant System Pressure in the Surtsey Test Facility, Sandia National Laboratory report NUREG/CR-5746, SAND99-1634, July 1999

[7] Fishburne E.S., Pergament H.S., The dynamics and radiant intensity of large hydrogen flames, 17th Int. Symposium on Combustion, 1978, pp. 1063-1073

[8] Wilhelm D., Transient Code Models for Low Pressure Corium Dispersion, Proc. of the OECD Workshop on Ex-Vessel Debris Coolability, Karlsruhe, Nov. 15-18, 1999, wissenschaftliche Berichte, FZKA-6475 (May 2000), pp. 45-53

[9] Wilhelm D., Substantiation of the Choice of the Cell Size for the Expansion Phase Calculations with AFDM, report STR/LTEM/96-46, CEA-Grenoble, France, September 1996

[10] Washington K.E., Williams D.C., Direct Containment Heating Models in the CONTAIN Code, Sandia National Laboratory report SAND94-1073, August 1995

[11] Pilch M.M., Allen M.D., Klamerus E.W., Resolution of the Direct Containment Heating Issue for All Westinghouse Plants with Large Dry Containments or Subatmospheric Containments, Sandia National Laboratory report NUREG/CR-6338, 1996